Supplementary Information

Robust CO_2-to-C_{2+} electrosynthesis on alkaline-earth/copper catalysts

Xintao Ma,[1] Peng Chen,[1,3] Rong Zhang,[1,3] Shuaiwei Jiang,[1] Zehui Xie,[1,3] Shuo Feng,[1] Yeyang Jia,[1] Kim Hung MAK,[1] Zhiqiang Zhao,[1] Hu Hong,[1,3,5] Shaoce Zhang,[1] Zhiquan Wei,[1] Zhanxi Fan,[6*] Qichun Zhang,[1*] Xia-Guang Zhang,[2*] Chunyi Zhi[1,3,4,5*]

[1]Department of Materials Science and Engineering, City University of Hong Kong, 83 Tat Chee Avenue, Kowloon, Hong Kong 999077, China

[2]Key Laboratory of Green Chemical Media and Reactions, Ministry of Education, Collaborative Innovation Center of Henan Province for Green Manufacturing of Fine Chemicals, School of Chemistry and Chemical Engineering, Henan Normal University, Xinxiang, 453007, China

[3]Department of Mechanical Engineering, The University of Hong Kong, Pokfulam, Hong Kong, China

[4]Materials Innovation Institute for Life Sciences and Energy (MILES), HKU-SIRI, Shenzhen 518048, China

[5]Center for Energy Storage, The University of Hong Kong, Pokfulam, Hong Kong, China

[6]Department of Chemistry, City University of Hong Kong, 83 Tat Chee Avenue, Kowloon, Hong Kong 999077, China

*Corresponding author: zhanxi.fan@cityu.edu.hk; qiczhang@cityu.edu.hk; zhangxiaguang@htu.edu.cn; cyzhi@hku.hk

Table of Supplementary Figures

Table of Supplementary Tables

Extended Methods

Calculations of CO_2RR performance parameters

The FE of the gaseous product was calculated by Eq. 1 as follows.

$$FE_{gas}\,(\%) = I_{gas}/\,I_{total} \times 100\% = z \times F \times P \times V_{gas} \times \varphi_{gas} / R / T / I_{total} \times 100\% \quad (1)$$

where I_{gas} and I_{total} are the partial current density for a specific product and the total current density, respectively. The parameters of z, F, P, V_{gas}, $\varphi_{gas,}$ R, and T represent the number of the electron transferred, Faradaic constant (96485 C mol^{-1}), atmospheric pressure (101325 Pa), gas flow rate at the cathode side outlet of the flow cell, the volume fraction of the gaseous product, molar gas constant (8.314 J mol^{-1} K^{-1}), and temperature (298.15 K), respectively.

The FE of the liquid product was calculated by Eq. 2 as follows.

$$FE_{liquid}\,(\%) = Q_{liquid} / Q_{total} = F \times C_{liquid} \times V_{liquid} \times z / Q_{total} \times 100\% \quad (2)$$

where Q_{liquid} and Q_{total} are the partial charge to produce a specific liquid product and the total charge consumed in the electrolysis, respectively. F, C_{liquid}, V_{liquid}, and z represent the Faradaic constant, concentration of a specific liquid product, the volume of the electrolyte, and the number of electrons transferred for CO_2RR to produce a specific liquid product, respectively.

The formation rate ($f_{product}$) of a specific product was calculated by Eq. 3 as follows.

$$f_{product}\,(\text{mmol cm}^{-2}\,\text{h}^{-1}) = Q_{product} / 1000 / F / z / t / S \times FE_{product} \quad (3)$$

where $Q_{product}$, F, z, t, and S represent the partial charge transferred for CO_2RR to produce a specific product, Faradaic constant, concentration of a specific product, the

number of electrons transferred for CO_2RR to a specific product, the electrolysis time, and the geometric area of the working electrode (cm^2), respectively.

The CO_2 single-pass conversion efficiency (SPCE) was calculated by Eq. 4 as follows.

$$SPCE = \frac{60\ s \times \sum\ (I \times x_i \times FE_i \div (N_i \times F)}{flow\ rate\ (L\ min^{-1}) \times 1\ (\text{min})\ \div 24.5\ (L\ min^{-1})} \quad (4)$$

where I is the current density, x_i is the mole ratio of CO_2 to produce a specific product, FE_i is the Faradaic efficiency of a specific product, N_i is the number of electrons transferred for CO_2 to produce a specific product.

The energy conversion efficiency (ECE) of a specific product was calculated by Eq. 5 as follows.

$$ECE = \sum E_0 \times FE / E_{app} \quad (5)$$

Where E_0, FE and E_{app} are the thermodynamic potential (Supplementary Table 4), the FE of the specific product and the applied cell voltage, respectively.

Calculations of the water consumption rate in the cathodic reaction

The water consumption rate in CO_2RR (f_{CO2RR}) was calculated by Eq. 6 as follows

$$f_{CO2RR}\ (\text{mmol h}^{-1}\ \text{cm}^{-2}) = \sum f_{product} \times n_{H2O} / n_{product} \quad (6)$$

where $f_{product}$ and n_{H2O} / $n_{product}$ represent the product formation rate of CO_2RR and the molar ratio of reaction, respectively.

The water consumption rate in HER (f_{HER}) was calculated by Eq. 7 as follows

$$f_{HER}\ (\text{mmol h}^{-1}\ \text{cm}^{-2}) = f_{H2} \times n_{H2O} / n_{H2} \quad (7)$$

where f_{HER} and n_{H2O} / n_{H2} represent the hydrogen formation rate of HER and the molar ratio of reactions (as shown in Supplementary Table 1), respectively.

The total water consumption rate (f_{total}) was calculated by Eq. 8 as follows

$$f_{total}\,(\text{mmol h}^{-1}\text{ cm}^{-2}) = f_{HER} + f_{CO2RR} \quad (8)$$

Electrochemical *operando* Raman spectroscopy

The *operando* Raman measurements were conducted on a LabRAM HR Evolution Raman Microscope (Horiba Jobin Yvon) within a modified flow cell setup. The GDE loaded with catalyst served as the working electrode, an Ag/AgCl electrode and a Ni foam were used as the reference electrode and the counter electrode, respectively. In the flow cell, a 1 M KOH aqueous solution was continuously circulated through the cathodic and anodic chambers using peristaltic pumps at a flow rate of 10 mL min^{-1}. *Operando* Raman tests were performed by applying various potentials, ranging from the open–circuit potential (OCP) to –1.2 V versus RHE, to the working electrode. A 632.8 nm laser was used for the Raman measurements, and the Raman signals were recorded with an accumulation time of 30 seconds and an average of two scans.

Electrochemical in situ ATR-FTIR spectroscopy

Electrochemical in situ ATR-FTIR measurements were performed to monitor the reaction intermediates of CO_2RR on a homemade H-cell (Supplementary Fig. 37). The electrolyte was degassed by bubbling Ar for at least 30 minutes before the

measurements. The catalyst was dropped onto a germanium ATR crystal coated with an Au film, which served as the working electrode. An Ag/AgCl electrode and a Pt wire were used as the reference electrode and counter electrode, respectively. The homemade electrolyzer was integrated into the NICOLET 6700 FTIR spectrometer equipped with an MCT detector cooled by liquid nitrogen. CO_2-saturated 1 M KCl and 1 M KOH aqueous solutions served as the cathodic and anodic electrolytes, respectively. A continuous potential ranging from OCP to –1.2 V at intervals of –0.1 V was applied; the IR signals were analyzed and identified by referencing standard samples, control experiments, and relevant literature. The single-bounce silicon crystal covered with an Au membrane was prepared by the following procedure. (1) NaOH (0.12 g), $NaAuCl_4 \cdot 2H_2O$ (0.23 g), NH_4Cl (0.13 g), Na_2SO_3 (0.95 g), and $Na_2SO_3 \cdot 5H_2O$ (0.62 g) were dissolved in H_2O (100 mL) solution A. (2) Monocrystal silicon was immersed in aqua regia ($V_{\text{concentrated HCl}} : V_{HNO3} = 1:1$) for 20 minutes and then polished using Al powder for at least 10 minutes. After washing three times with ultrapure water and acetone, the clean monocrystal silicon was obtained. (3) The above monocrystal silicon was immersed in a mixture of H_2SO_4 and H_2O_2 ($V_{\text{concentrated H2SO4}} : V_{H2O2} = 1:1$) for at least 20 minutes. (4) After washing three times with ultrapure water, the above monocrystal silicon was immersed in a 40 wt% NH_4F aqueous solution and washed three times with ultrapure water. (5) The monocrystal silicon was immersed in a mixture of 15 mL of solution A and 3.4 mL 2% NH_4F aqueous solution. (6) After 5 minutes, Au-coated monocrystalline silicon was obtained.

Electrochemical online DEMS test

Operando Differential electrochemical mass spectrometry (DEMS) was conducted on a custom-made Linglu DEMS flow cell. The DEMS capillary flow cell is distinguished by a well-defined electrolyte flow profile across the working electrode. Reaction products are transported to the liquid-vacuum interface through a 0.15 mm glass capillary. The accumulation of high-concentration aliquots in the vicinity of the catalyst surface, combined with the enhanced liquid–vacuum interface, enables rapid and high-sensitivity detection of gaseous products. The superior performance of the DEMS capillary flow cell stems from the distributed flow within the hydrophobic membrane compartment, also known as cyclonic flow. The superior performance of the DEMS capillary flow cell stems from the distributed flow within the hydrophobic membrane compartment, a flow pattern also referred to as cyclonic flow. The liquid-vacuum interface is facilitated by a PTFE hydrophobic membrane (pore size: 20 μm; thickness: 50 μm; Cobetter Co., Ltd., Cat. No. PF-002HS), which is commercially available from Hangzhou Cobetter Filtration Equipment Co., Ltd. After vaporization from the flow cell into the vacuum chamber, reaction products were detected using a PrismaTM quadrupole mass spectrometer (QMS 200, Pfeiffer-Vacuum). The vacuum chamber was equipped with two turbomolecular pumps (HiPace 80), which achieve an ultimate pressure of 10^{-6} mbar at the MS detectors. Each turbomolecular pump is outfitted with an independent baking system, supported by a membrane pump and an oil pump (coupled with a molecular sieve oil trap).

Electrochemical EPR measurements

The in situ electrochemical electron paramagnetic resonance (EPR) measurements were performed using a Bruker EMX Plus spectrometer, which operated at an approximate frequency of 9.6 GHz, with a sweep width of 100 G and an applied power of 3 mW. To capture active hydrogen radicals, 5,5-dimethyl-1-pyrroline N-oxide (DMPO), a molecular trapping agent, was employed; this reagent reacts with hydrogen radicals to form DMPO-H adducts, which are detectable via EPR spectroscopy. For a typical measurement, chronopotentiometry electrolysis was conducted on the cathode under Ar protection. Following 30 s of electrolysis, EPR signals were recorded. Each fresh cathode was initially tested in a CO-free solution and subsequently retested under identical conditions in a solution with CO purged.

Operando XAS measurements

The *operando* XAS experiments were conducted on a custom-made cell configuration. The working electrode consisted of a catalyst-loaded GDE, with an Ag/AgCl electrode serving as the reference electrode, and a Ni foam as the counter electrode. The electrolytes of the anode and cathode were both 1 M KOH aqueous solutions, which were circulated through their respective cell chambers via peristaltic pumps at a constant flow rate of 10 mL min^{-1}. The data were analyzed using the software package Athena.

Techno-economic analysis (TEA)

Our TEA model adheres to the general framework established in prior studies, and all relevant parameters are presented in Supplementary Table 5. Based on the flow cell model, our TEA calculations adopt a microchannel flow cell to conduct cost analysis and calculations. We estimated the costs of producing 100 tonnes of ethylene per day (32,850 tonnes per year, with a capacity factor of 0.9) over a 20-year factory life. We tested the microchannel flow cell voltage under different current densities (0.1, 0.2, 0.3, 0.4, 0.6, 0.8, 1.0, 1.2 A cm^{-2}) and conducted relevant calculations based on the cell voltage and current density corresponding to each current density.

Regarding the production of ethylene from CO_2, the corresponding chemical equations are listed below:

$$Cathode: 2CO_2 + 12\,e^- + 8H_2O \rightarrow C_2H_4 + 12OH^-$$

$$Anode: 4OH^- - 4e^- \rightarrow O_2 + 2H_2O$$

$$Overall: 2CO_2 + 2H_2O \rightarrow C_2H_4 + 3O_2$$

Thus, the production of 1 mol of ethylene (C_2H_4) demands 0.5 mol of CO_2 and 0.5 mol of H_2O. Nevertheless, given that the selectivity for CO_2 conversion to ethylene is below 100%, a CO_2 input exceeding 1 mol is thus required.

Electricity

The production rate of ethylene in moles per second is:

$$C2H4\ production\ (mol\ s^{-1}) = \frac{C2H4\ production\ (\frac{g}{day})}{M_{C2H4}\ (\frac{g}{mol})} = \frac{100 \times \frac{10^6\ g}{day}}{28\ g\ mol^{-1} \times 86400\ s\ day^{-1}} =$$

41.34 $mol\ s^{-1}$

Accounting for electron loss resulting from an FE of less than 100%, we calculate the current required for ethylene production at the target output rate:

$$I_{total}\ \text{(A)} = \frac{C2H4\ production\ (mol\ s^{-1}) \times n \times F}{FE_{C2H4}} = \frac{41.336\ mol\ s^{-1} \times 12 \times 96485\ sA\ mol^{-1}}{68.63\ \%} =$$

69,735, 717.64 A

We multiply this value by the experimentally obtained microchannel flow cell voltage of 3.38 V to calculate the consumed power:

$Power\ (kW) = I_{total}$ (A) × V_{cell} (V)= 69,735,717.64 × 3.38 = 235,706.73 kW

We multiply the power consumption by 24 hours to calculate the energy consumed for producing 100 tonnes of ethylene. By multiplying the required energy by the electricity price (1 ¢/kWh), we derive the cost per tonne of ethylene:

$$Cost_{electricity}(\frac{\$}{tonne\ C2H4}) = \frac{Power \times 24\ h \times price_{electricity}}{C2H4\ production} = \frac{235{,}706.73\ kW \times 24\ h \times \frac{0.01\ \$}{kWh}}{100\ (tonne\ C2H4\ day^{-1})} =$$

$$\frac{\$\ \mathbf{565.70}}{\boldsymbol{tonne\ C2H4}}$$

Electrolyzer capital cost

The reference cost for the electrolyzer is 450 $/kW, with a reference current density of 400 mA cm^{-2}. By multiplying this value by the electrolyzer's unit price (450 $/kW) and adjusting for the actual input current density (1000 mA cm^{-2}), we derive the total cost of the electrolyzer:

$$Cost_{Total\ Electrolyzer}\ (\$) = Power\ Consumed\ (kW)\ \times\ Cost_{Electrolyzer}\ (\$) \times \frac{base\ current\ density\ (mA\ cm^{-2})}{input\ current\ density\ (mA\ cm^{-2})} = 235{,}706.73\ kW\ \times 450\ \$\ kW^{-1}\ \times \frac{400\ (mA\ cm^{-2})}{1000\ (mA\ cm^{-2})} =$$

$\$\ 42{,}427{,}210.61$

The above figure represents the lump-sum total cost of the electrolyzer, which needs to be converted into the cost per tonne of ethylene.

For all capital costs, the same approach, transforming long-term investments into daily costs, is adopted. This method relies on a capital recovery factor (CRF), which is calculated using a discount rate (i) of 7% and a material lifespan of 20 years.

$$CRF_{electrolyzer} = \frac{i\,(1+i)^{lifetime}}{(1+i)^{lifetime}-1} = \frac{0.07 \times (1.07)^{20}}{(1.07)^{20}-1} = 0.0944$$

Subsequently, we multiply the total capital cost of the electrolyzer with the CRF and then divide the product by the plant's annual operating days and daily ethylene output. For all calculation processes, we adopt the assumption that the plant operates with a capacity factor of 0.9.

$$Cost_{electrolyzer}\ \left(\frac{\$}{tonne\ C2H4}\right) = \frac{CRF_{electrolyzer} \times Cost_{electrolyzer}\ (\$)\ (mA\ cm^{-2})}{Capacity\ factor \times 365\ (days\ year^{-1}) \times production\ (tonne\ C2H4\ day^{-1})}$$

$$= \frac{0.0944 \times \$42{,}427{,}210.61}{0.9 \times 365\ day\ year^{-1} \times 100\ (tonne\ C2H4\ day^{-1})} = \frac{\mathbf{\$121.91}}{\boldsymbol{tonne\ C2H4}}$$

Catalyst and membrane costs

For the costs of the catalyst and membrane, we adopt the assumption that they account for 5% of the electrolyzer cost. By leveraging a 5-year service life of the catalyst and membrane, we can calculate the corresponding cost per tonne of ethylene:

$$CRF_{Catalyst\ and\ membrane} = \frac{i\,(1+i)^{lifetime}}{(1+i)^{lifetime}-1} = \frac{0.07\times(1.07)^{5}}{(1.07)^{20}-1} = 0.2439$$

$$Cost_{Catalyst\ and\ membran}\left(\frac{\$}{tonne\ C2H4}\right) =$$

$$\frac{CRF_{Catalyst\ and\ membrane}\times Cost_{Catalyst\ and\ membrane}(\$)\times 5\%}{Capacity\ factor\times 365\ days\ year^{-1}\times production\ (tonne\ C2H4\ day^{-1})} =$$

$$\frac{0.2439\times \$42{,}427{,}210.61\times 5\%}{0.9\times 365\ day\ year^{-1}\times 100\ (tonne\ C2H4\ day^{-1})} = \frac{\$15.75}{\boldsymbol{tonne\ C2H4}}$$

Cathode gas separation

Gaseous by-products (H_2) are removed from the CO_2 outlet stream, facilitating the recirculation of unreacted CO_2. For the calculation of gaseous separation costs, we rely on the estimated values derived from a referenced pressure-swing adsorption (PSA) system.

$$C_2H_4\ Flow\ rate\ (m^3\ h^{-1}) = \frac{C_2H_4\ production\ rate\times 24.5\times 10^{-3}}{P} =$$

$$\frac{\frac{100\times 10^{6}}{28\times 24}(mol\ h^{-1})\times 24.5\times 10^{-3}}{1\ atm} = 3645.83\ (m^3\ h^{-1})$$

$$Output\ CO_2\ Flow\ Rate\ (m^3\ h^{-1}) = \frac{C_2H_4\ flow\ rate\times(1-Single\ pass\ rate)}{Single\ pass\ rate} =$$

$$32{,}812.47\ m^3\ h^{-1}$$

$$Output\ H_2\ Flow\ Rate\ (m^3\ h^{-1}) = \frac{Total\ current\ (A\ s^{-1})\times FE_{H2}\times 3600\times 8.314\times 298.15}{96485\times 2\times 1\ atm} =$$

$$2301.29\ (m^3\ h^{-1})$$

The total of the flow rates of gaseous by-products and unreacted CO_2 serves to calculate the gaseous separation cost:

The total flow rate $(m^3\ h^{-1}) = C_2H_4\ Flow\ rate + H_2\ Flow\ rate + Unreacted\ CO_2\ Flow\ Rate = 39{,}698.31\ (m^3\ h^{-1})$

$$Gas\ Separation\ Operational\ Cost\ \left(\frac{\$}{tonne}\right) =$$

$$\frac{Total\ Flow\ Rate \times Reference\ PSA\ cost \times electricity\ price}{target\ output\ production\ of\ C_2H_4} = 39{,}698.31\ (m^3\ h^{-1})\ \times$$

$$24\ h\ day^{-1}\ \times 0.01\ \$\ kWh^{-1} \div 100\ tonne\ C_2H_4\ day^{-1} = \$23.82\ \text{tonne}\ C_2H_4$$

$$Gas\ Separation\ Capital\ Cost\ \left(\frac{\$}{tonne}\right) =$$

$$\frac{Reference\ PSA\ capital\ cost \times \left(\frac{Total\ flow\ rate}{Reference\ capacity}\right)^{scaling\ factor} \times CRF}{Capacity\ factor \times 365 \times target\ output\ production} = \$75.19\ \text{tonne}\ C_2H_4$$

$$Total\ Gas\ Separation\ Cost\ \left(\frac{\$}{tonne}\right) = Gas\ Separation\ Operational\ Cost +$$

$$Gas\ Separation\ Capital\ Cost = \mathbf{\$99.01\ tonne\ C_2H_4}$$

Input CO_2

Initially, under the assumption that there are no losses, we compute the input CO_2 required to produce 100 tonnes of ethylene.

$$CO_2\ required\ (tonne\ CO_2\ day^{-1}) = product\ output\ (tonne\ product\ day^{-1})\ \times$$

$$\frac{M_{CO2}}{M_{product}} \times molar\ ration\ \left(\frac{CO_2}{product}\right) = 78.6\ tonne\ CO_2\ day^{-1}$$

Here, we multiply this value by a market price for CO_2, which is $30/tonne.

$$Cost_{input\ CO2}\ \left(\frac{\$}{tonne\ C2H4}\right) = \frac{\$30}{tonne\ CO2} \times 78.6\ tonne\ CO_2\ day^{-1}\ \times$$

$$\frac{1}{100\ tonne\ C_2H_4\ day^{-1}} = \mathbf{\$23.6\ tonne\ C_2H_4}$$

Input water

The amount of water required was calculated using the same method outlined above:

$$H_2O\ required\ \left(\frac{tonne\ H_2O}{day}\right) = product\ ouput\ (tonne\ product\ day^{-1})\ \times$$

$$\frac{M_{H2O}}{M_{product}} \times molar\ ration\ \left(\frac{H_2O}{product}\right) = 32.1\ tonne\ H_2O\ day^{-1}$$

Here, we multiply this value by the water cost ($5/tonne) and then divide by our daily ethylene production. The resulting cost of the input water is:

$$Cost_{input\ H2O}\ \left(\frac{\$}{tonne\ C_2H_4}\right) = 5\frac{\$}{tonne\ H_2O} \times 32.1\ \frac{tonne\ H_2O}{day} \times \frac{1}{100\ tonne\ C_2H_4\ day^{-1}} = \frac{\$\mathbf{1.61}}{\boldsymbol{tonne\ C_2H_4}}$$

Electrolyte cost

The electrolyte used herein is 1.0 M KOH. With the adoption of a fixed volume ratio, 100 L of electrolyte per square meter of electrolyzer, we are able to determine the total volume of electrolyte required.

$$Volume_{electrolyte}\ (L) = Surface\ area_{electrolyzer}\ (m^2) \times 100\ (L\ m^{-2}) = \frac{Total_{current}\ (A\ s^{-1})}{Current\ density\ (mA\ cm^{-2}) \times (\frac{100\ cm}{1\ m})^2} \times 100\ (L\ m^{-2}) = \frac{Total_{current}\ (A\ s^{-1})}{1.0\ (A\ cm^{-2}) \times (\frac{100\ cm}{1\ m})^2} \times 100\ (L\ m^{-2}) = \frac{69{,}735{,}717.64}{1 \times 100^2} \times 100 = 697{,}357.18\ L$$

$$Mass_{salt} = molarity_{salt}\ (mol\ L^{-1}) \times Volume_{electrolyte}\ (L) \times molecular\ weight\ (g\ mol^{-1}) = 1 \times 697{,}357.18 \times 56 = 39{,}052{,}001.88\ g$$

$$Cost_{electrolyte}\ (\$) = Mass_{salt}\ (tonne) \times price_{salt}\ \left(\frac{\$}{tonne}\right) + Volume_{water}\ (L) \times price_{water}\ \left(\frac{\$}{tonne}\right) = 39.05\ tonne \times 790\ \frac{\$}{tonne} + 697{,}357.18\ L \times \frac{1}{1000}\ \frac{tonne}{L} \times 5 \times \frac{\$}{tonne} = \$34{,}336.29$$

To derive the cost per tonne of ethylene, we calculated the updated capital recovery factor (CRF) of 1.07 based on the assumption that the electrolyte has a one-year lifespan. The electrolyte cost per tonne of ethylene is as follows:

$$Cost_{electrolyte}\left(\frac{\$}{tonne\ C_2H_4}\right) = \frac{CRF_{electrolyzer} \times Cost_{electrolyte}\ (\$)}{Capacity\ factor \times 365\left(\frac{days}{year}\right) \times production\ (\frac{tonne\ C_2H_4}{day})} = \frac{1.07 \times \$34{,}336.29}{0.9 \times 365\left(\frac{days}{year}\right) \times 100\ (\frac{tonne\ C_2H_4}{day})} = \mathbf{\$1.12\ tonne\ C_2H_4}$$

Balance of plant and installation

All capital costs are adjusted proportionally to calculate the cost of peripheral equipment for the electrolyzer and separation units. We adopt assumptions of a 50% balance of plants (BOP) and a Lang factor of 1. To determine the total capital costs, we add up the capital costs of the electrolyzer, membrane & catalyst, and cathode separation equipment.

$$Cost_{Total\ Capital}\left(\frac{\$}{tonne\ C_2H_4}\right) = Electrolyzer\ cost + Catalyst\ cost +$$

$$PSA\ capital\ cost = 121.97 + 15.76 + 75.19 = \frac{\$212.92}{tonne\ C_2H_4}$$

$$Cost_{installation}\left(\frac{\$}{tonne\ C_2H_4}\right) = Lang\ Factor\ \times\ Cost_{Total\ Capital} = 1\ \times \frac{\$212.92}{tonne\ C_2H_4} = \frac{\mathbf{\$212.92}}{\mathbf{tonne\ C_2H_4}}$$

$$BOP\left(\frac{\$}{tonne\ C_2H_4}\right) = BOP\ Factor\ \times Cost_{Total\ Capital} = 0.5\ \times \frac{\$212.92}{tonne} = \frac{\mathbf{\$106.46}}{\mathbf{tonne\ C_2H_4}}$$

Other operating costs

To account for the extra operating costs related to factory operations (including labor and maintenance), we have included an additional cost equivalent to 10% of the electricity cost:

$$Cost_{other\ operation}\left(\frac{\$}{tonne\ C_2H_4}\right) = Cost_{electricity}\left(\frac{\$}{tonne\ C_2H_4}\right) \times 0.10 = \frac{\mathbf{\$56.6}}{\mathbf{tonne\ C_2H_4}}$$

Total cost for one tonne of ethylene

By adding up all the above costs, we derive the cost of producing one tonne of ethylene in an electrolyzer:

$$Cost_{Ethylene} = Cost_{Electricity} + Cost_{Electrolyzer} + Cost_{Catalyst\ and\ membrane} + Cost_{Gas\ separation} + Cost_{CO_2} + Cost_{Water} + Cost_{Electrolyte} + BOP + Cost_{Operation} + Cost_{Installation} = 565.7 + 121.91 + 15.75 + 99.01 + 23.58 + 1.61 + 1.12 + 106.46 + 56.6 + 212.92 = \mathbf{\$1204.66\ tonne\ C_2H_4}$$

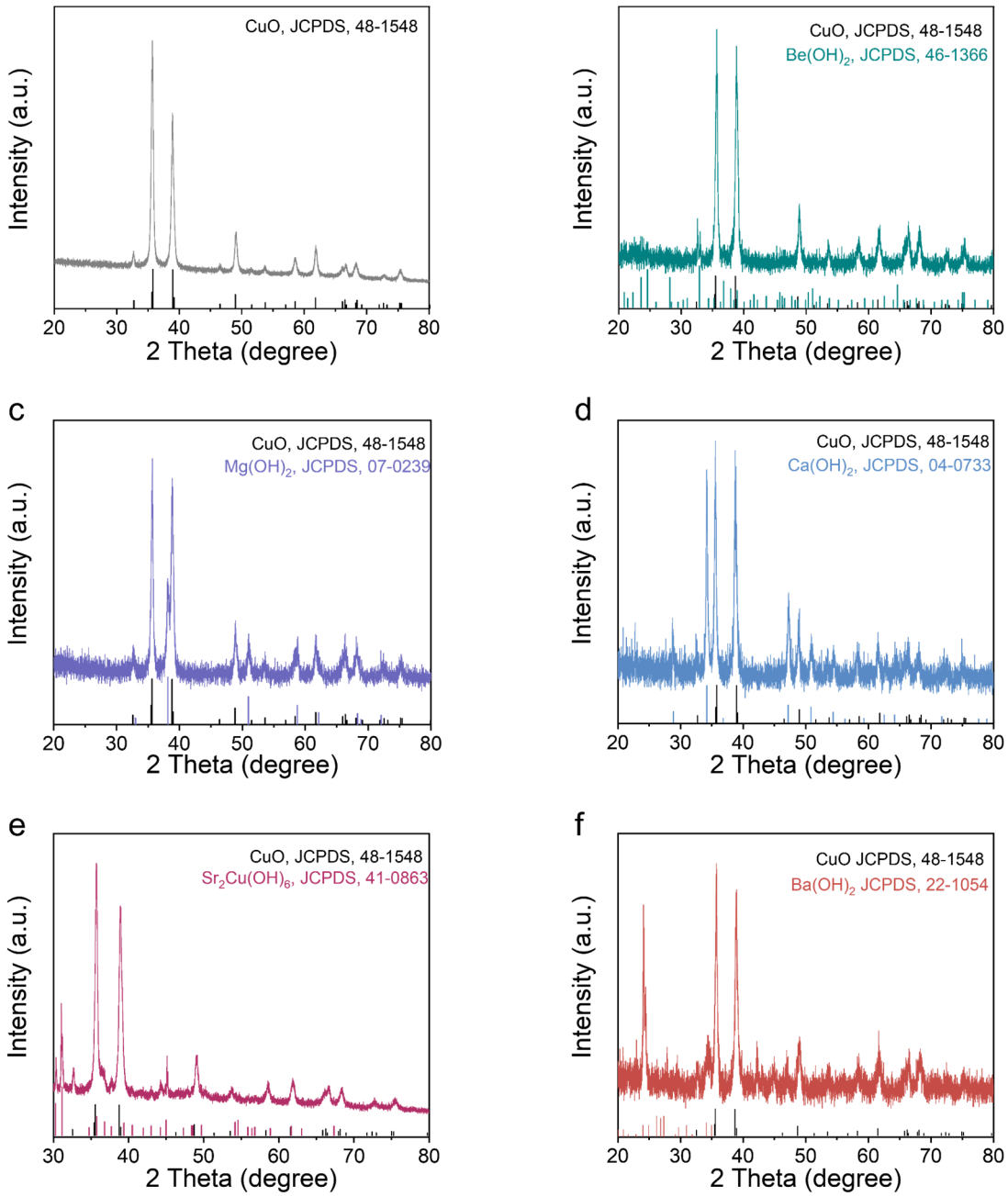

Supplementary Fig. 1 | XRD patterns of precursors. a, CuO. **b,** $Be(OH)_2$/CuO. **c,** $Mg(OH)_2$/CuO. **d,** $Ca(OH)_2$/CuO. **e,** $Sr_2Cu(OH)_6$/CuO. **f,** $Ba(OH)_2$/CuO. For ease of description, we denoted the corresponding catalyst precursors as CuO, Be-CuO, Mg-CuO, Ca-CuO, Sr-CuO, and Ba-CuO, respectively.

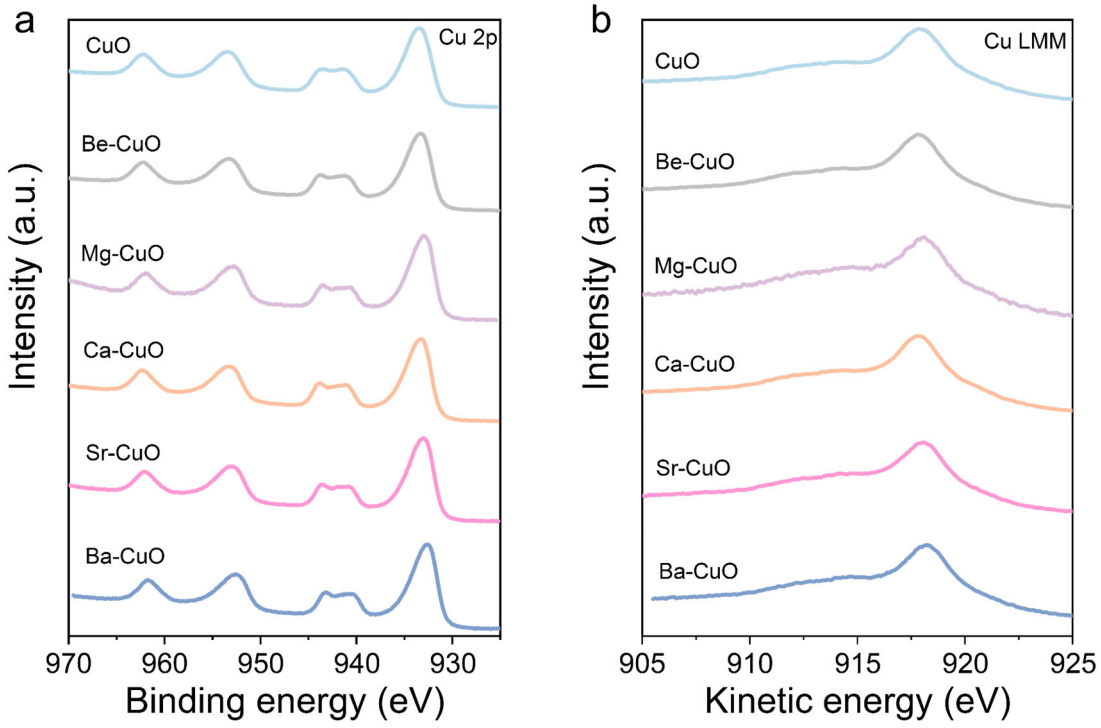

Supplementary Fig. 2 | Cu 2p and Cu LMM XPS spectra for X-CuO precursors. **a,** Cu 2p spectra. **b,** Cu LMM spectra. The chemical states of Cu in the X-CuO precursors were further investigated by XPS. The Cu 2p spectra display distinct shake-up satellite peaks alongside the main spin-orbit doublets, which unequivocally identified the copper species as Cu^{2+}. This conclusion is further supported by the Cu LMM Auger spectra, which exhibit shapes and kinetic energies typical of CuO. Thus, it can be concluded that the Cu oxidation state is well-maintained in all X-CuO precursors regardless of the alkaline-earth-metal-hydroxide modification.

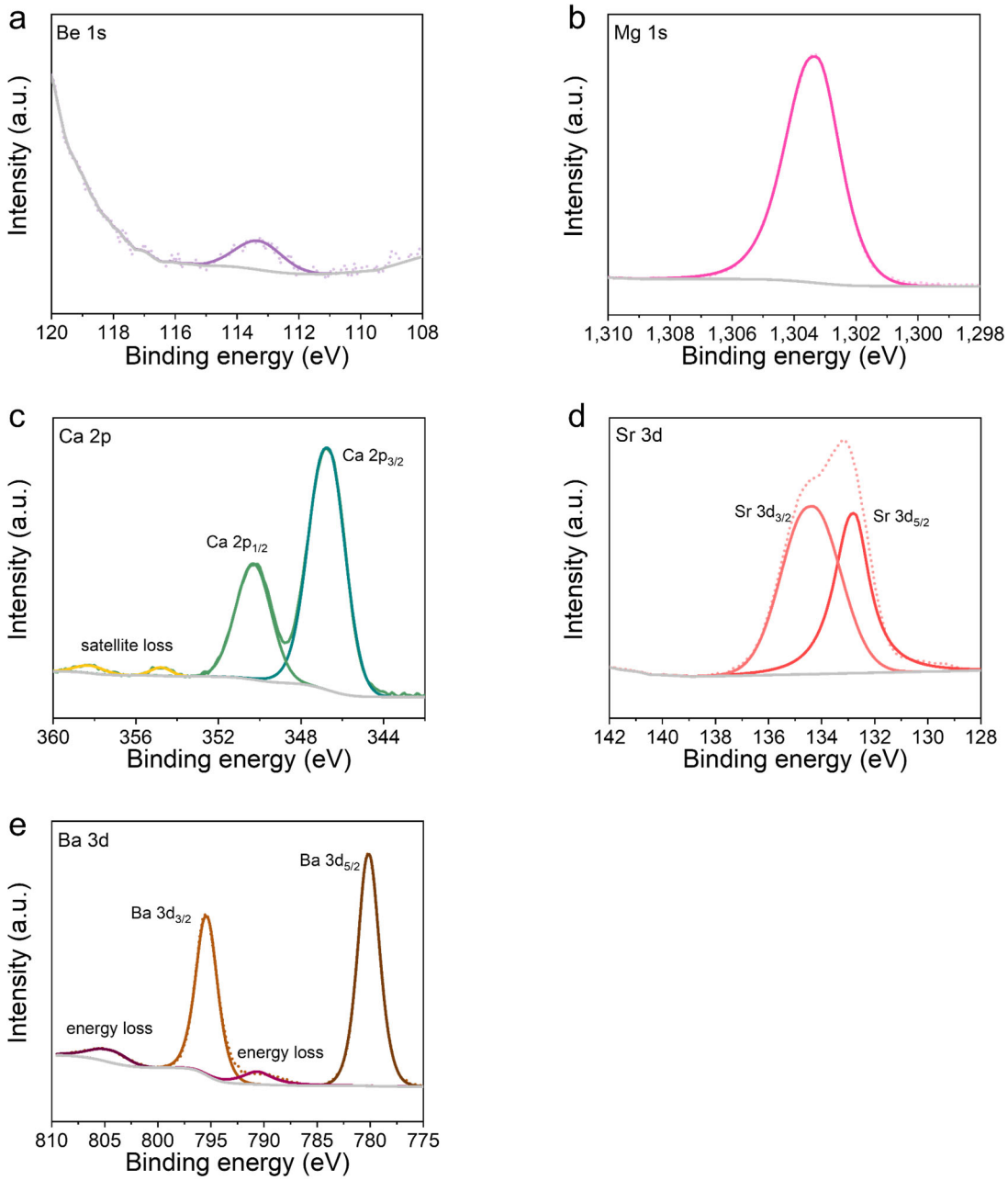

Supplementary Fig. 3 | Alkaline earth metal XPS spectra for X-CuO precursors.

a, Be 1s spectra of Be-CuO. **b,** Mg 1s spectra of Mg-CuO. **c,** Ca 2p spectra of Ca-CuO. **d,** Sr 3d spectra of Sr-CuO. **e,** Ba 3d spectra of Ba-CuO.

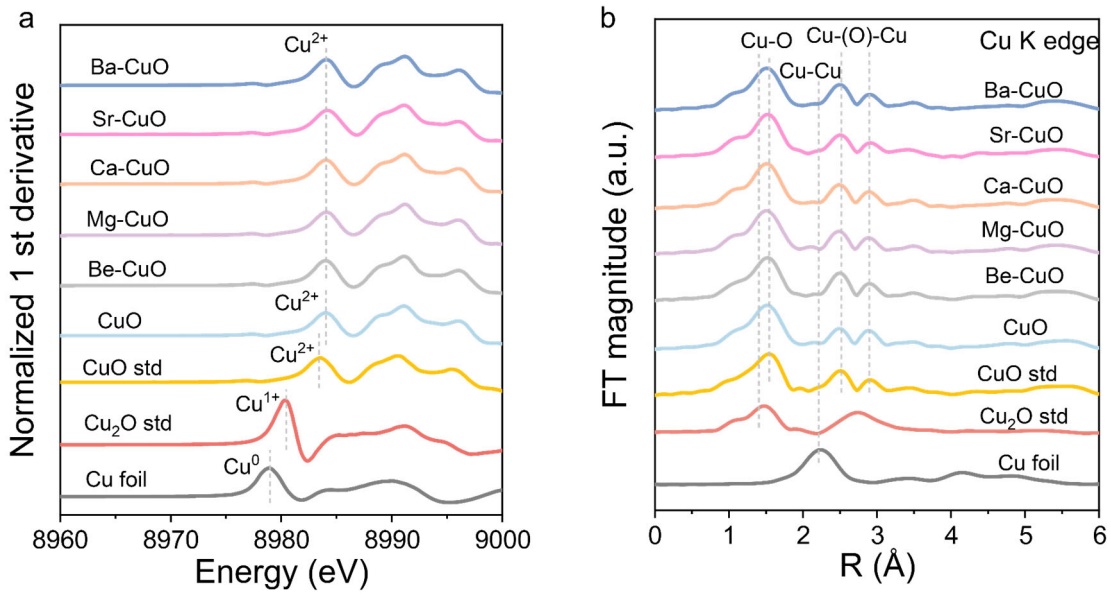

Supplementary Fig. 4 | X-ray absorption near-edge structure (XANES) spectra. a, First derivatives of the Cu K-edge XANES spectra of X-CuO precursors and of commercial Cu, Cu_2O and CuO as references. **b,** Corresponding k^2-weighted Fourier-transformed extended X-ray absorption fine structure (k^2-FT EXAFS) R-space spectra.

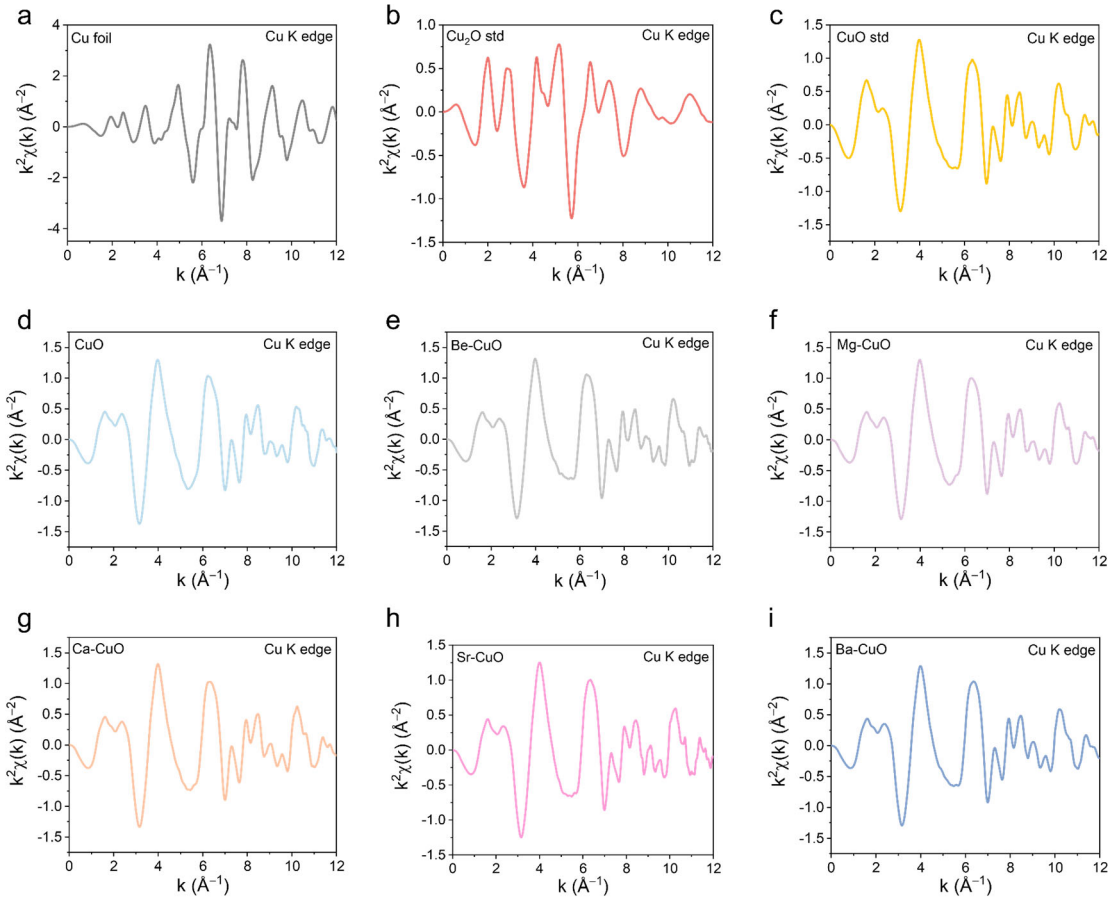

Supplementary Fig. 5 | k-space spectra of ex situ Cu K-edge XANES of different catalysts and the references. a, Cu foil. **b,** Cu_2O std. **c,** CuO std. **d,** CuO. **e,** Be-CuO. **f,** Mg-CuO. **g,** Ca-CuO. **h,** Sr-CuO. **i,** Ba-CuO.

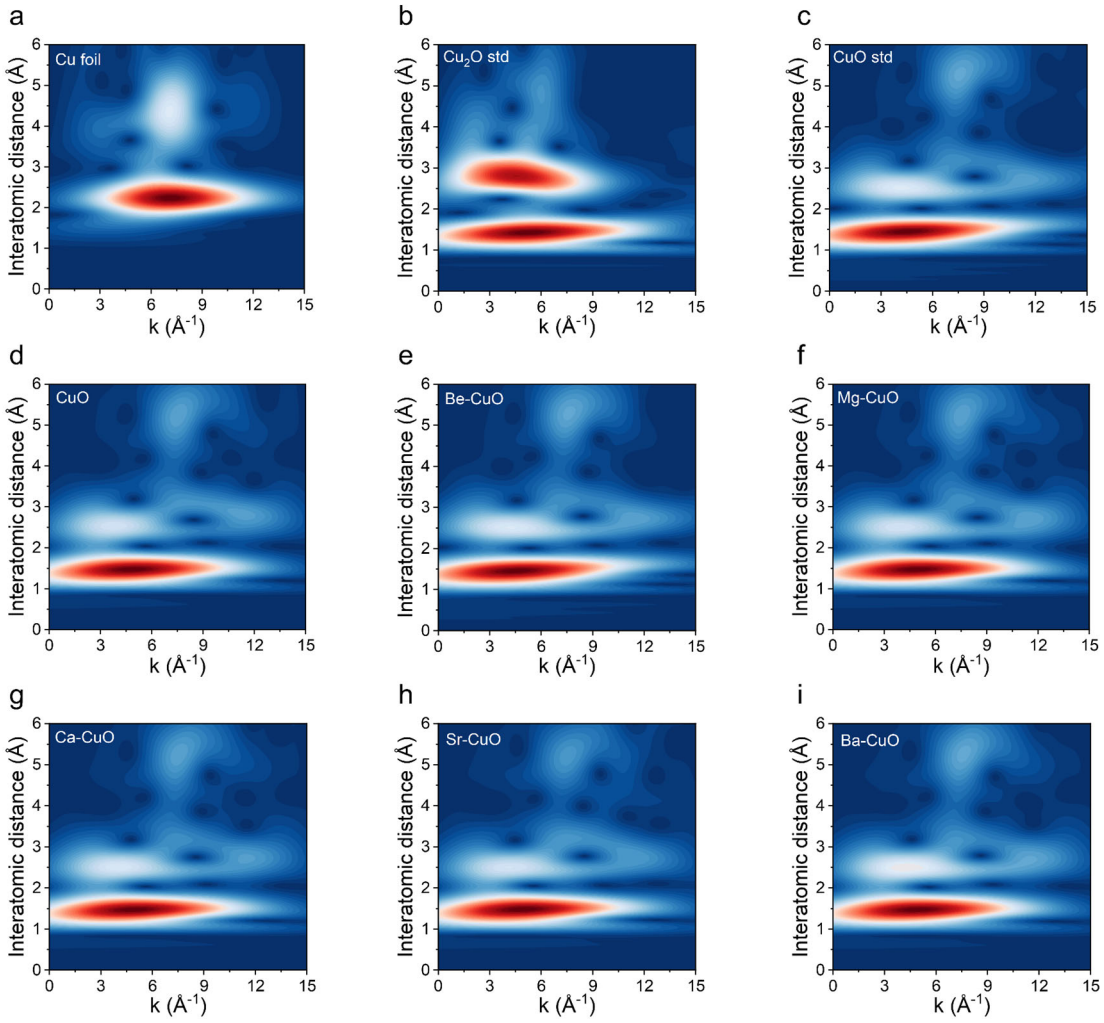

Supplementary Fig. 6 | Wavelet transform-EXAFS of as-prepared precursors and references. a, Cu foil. **b,** Cu_2O std. **c,** CuO std. **d,** CuO. **e,** Be-CuO. **f,** Mg-CuO. **g,** Ca-CuO. **h,** Sr-CuO. **i,** Ba-CuO.

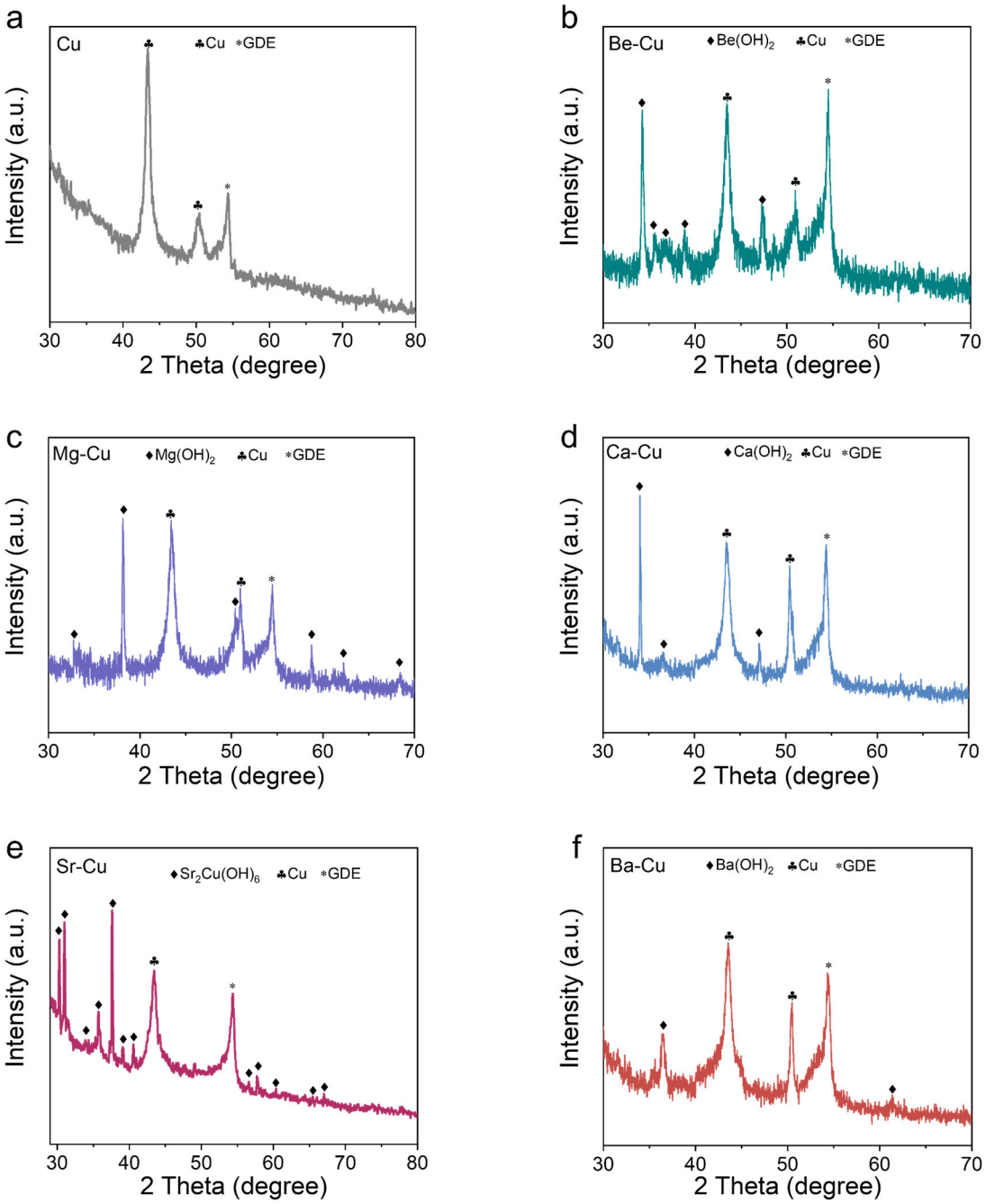

Supplementary Fig. 7 | XRD patterns of X-Cu catalysts. a, Cu. **b,** $Be(OH)_2$/Cu. **c,** $Mg(OH)_2$/Cu. **d,** $Ca(OH)_2$/Cu. **e,** $Sr_2Cu(OH)_6$/Cu. **f,** $Ba(OH)_2$/Cu. For ease of description, we denoted the corresponding catalyst precursors as Cu, Be-Cu, Mg-Cu, Ca-Cu, Sr-Cu, and Ba-Cu, respectively.

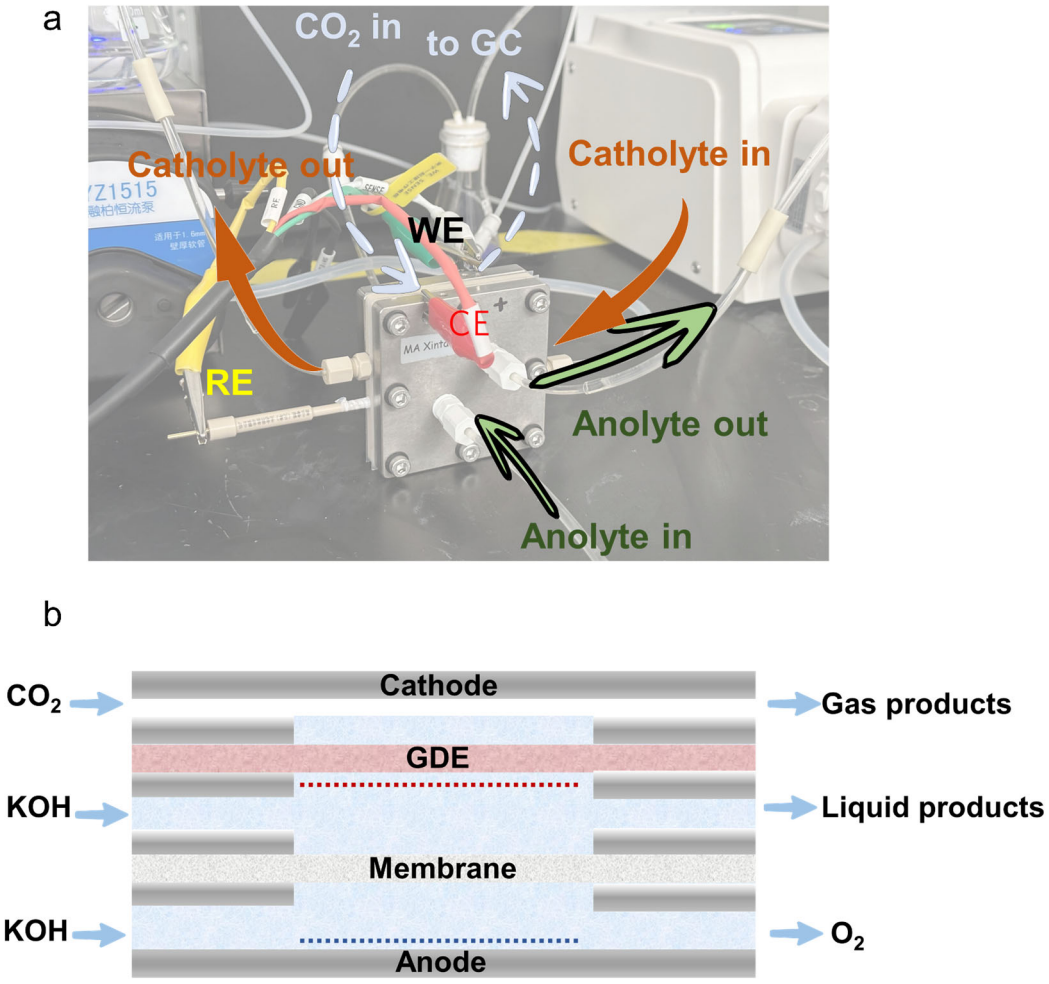

Supplementary Fig. 8 | Photograph and schematic illustration of the homemade flow cell used for CO_2RR measurements. a, Digital photo of the homemade flow cell. **b,** Schematic setup of the flow cell. The red and blue dotted lines represent the cathode and anode catalysts, respectively. The catholyte and anolyte chambers were separated by a FAB-PK-130 anion-exchange membrane (Fumasep).

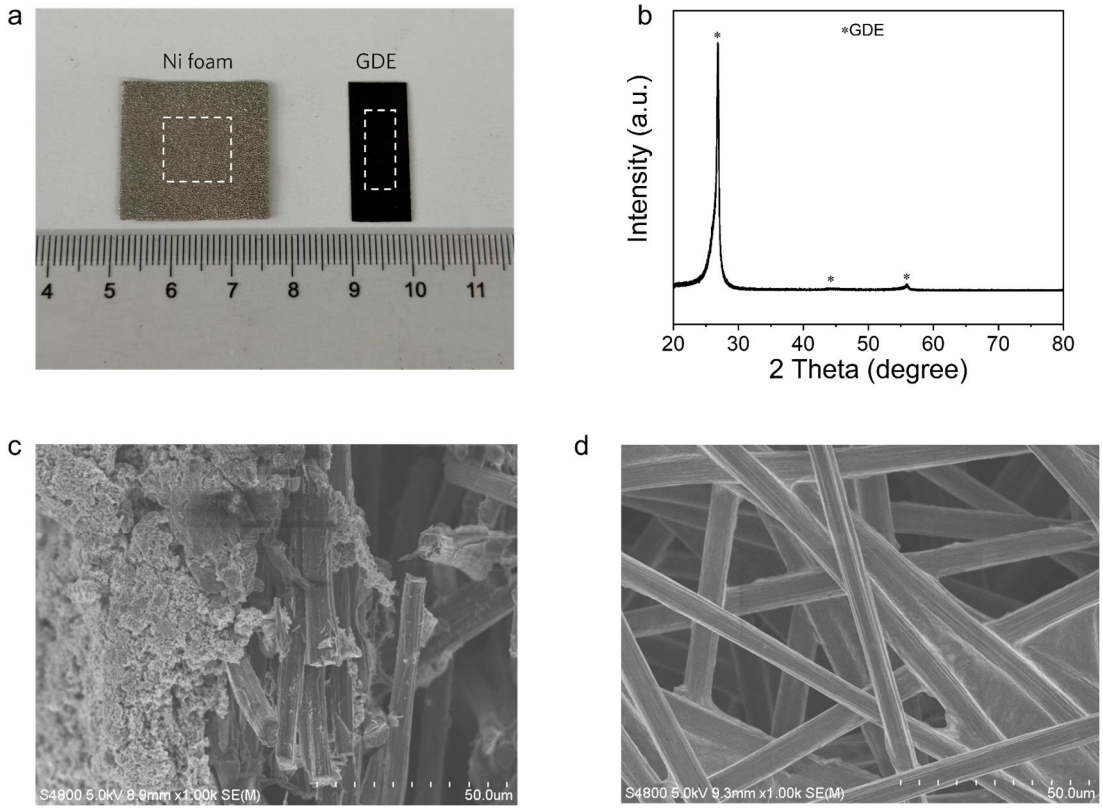

Supplementary Fig. 9 | Structural characterization of the electrodes used in the homemade flow cell. a, Photographs of the anode catalyst Ni foam and cathode GDE, the effective areas of Ni foam are 1×1 cm^2 and 0.5×2 cm^2 for GDE, which were marked with dotted boxes. **b,** XRD pattern of GDE. **c, d,** SEM images of the side and reverse sides of the GDE, respectively.

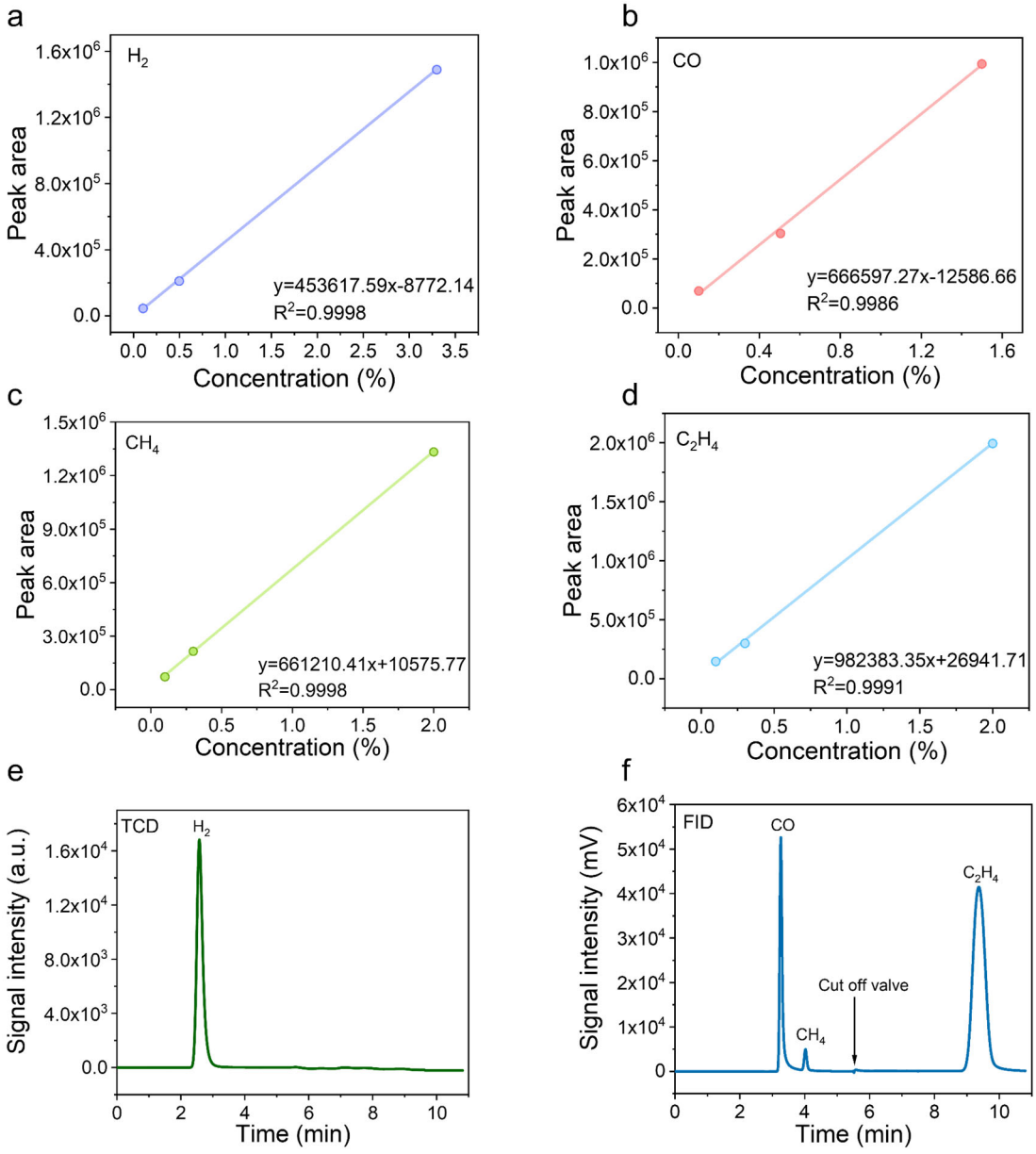

Supplementary Fig. 10 | Linear relationship between the gas product concentration and the peak area of GC. a, H_2. **b,** CO. **c,** CH_4. **d,** C_2H_4. Representative GC spectra for CO_2RR on the Cu catalyst at 1.0 A cm^{-2} for 10 mins. **e,** The thermal conductivity detector (TCD) was used to identify the H_2 product. **f,** The flame ionization detector of (FID) was used to identify the CO, CH_4, and C_2H_4 products.

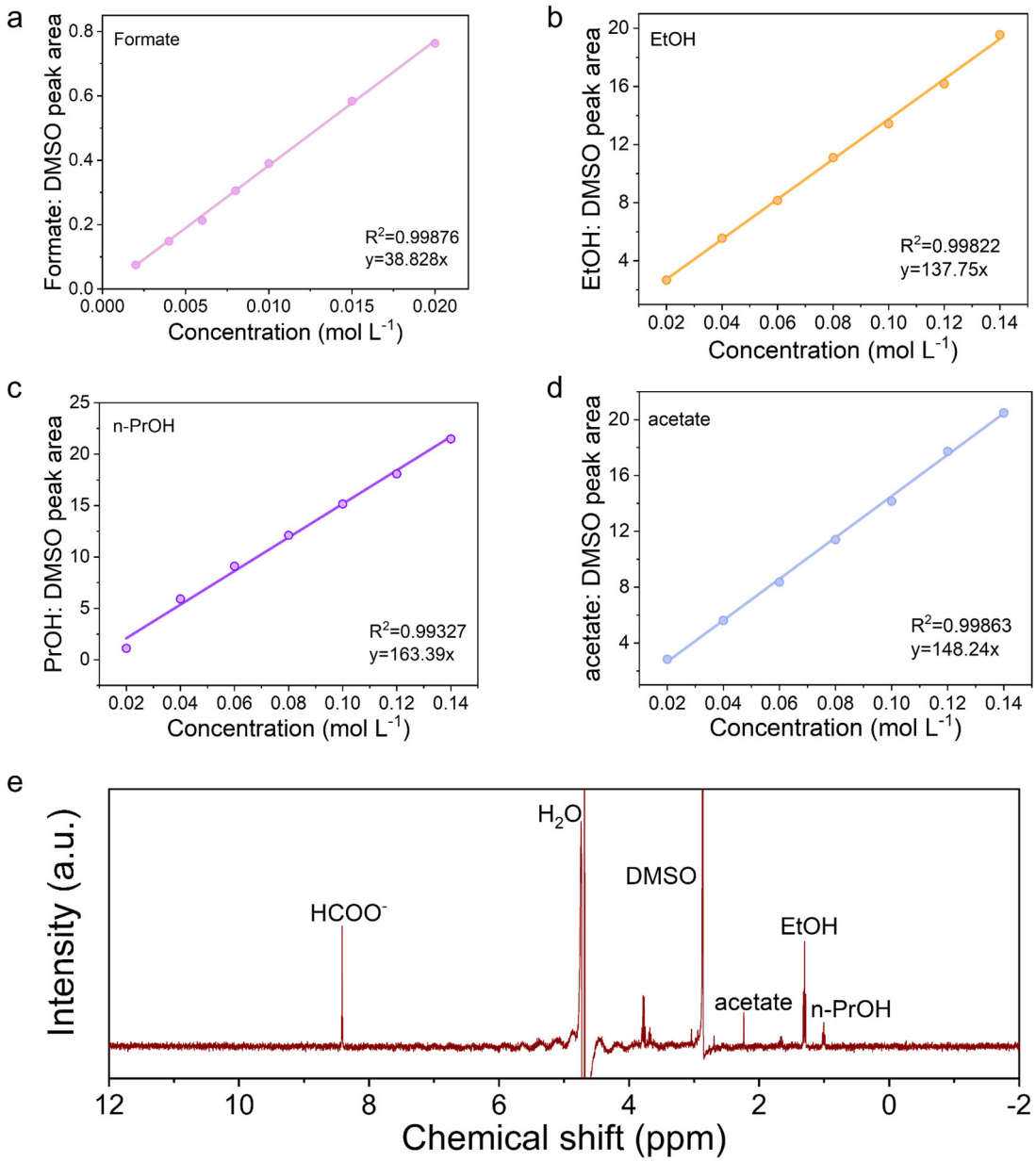

Supplementary Fig. 11 | Linear relationship between the liquid products concentration and relative area versus DMSO internal standard. a, Formate. **b,** EtOH. **c,** *n*-PrOH. **d,** acetate. **e,** Representative ^{1}H NMR spectra of the electrolyte after CO_2RR at 1.0 A cm^{-2} on Cu catalyst.

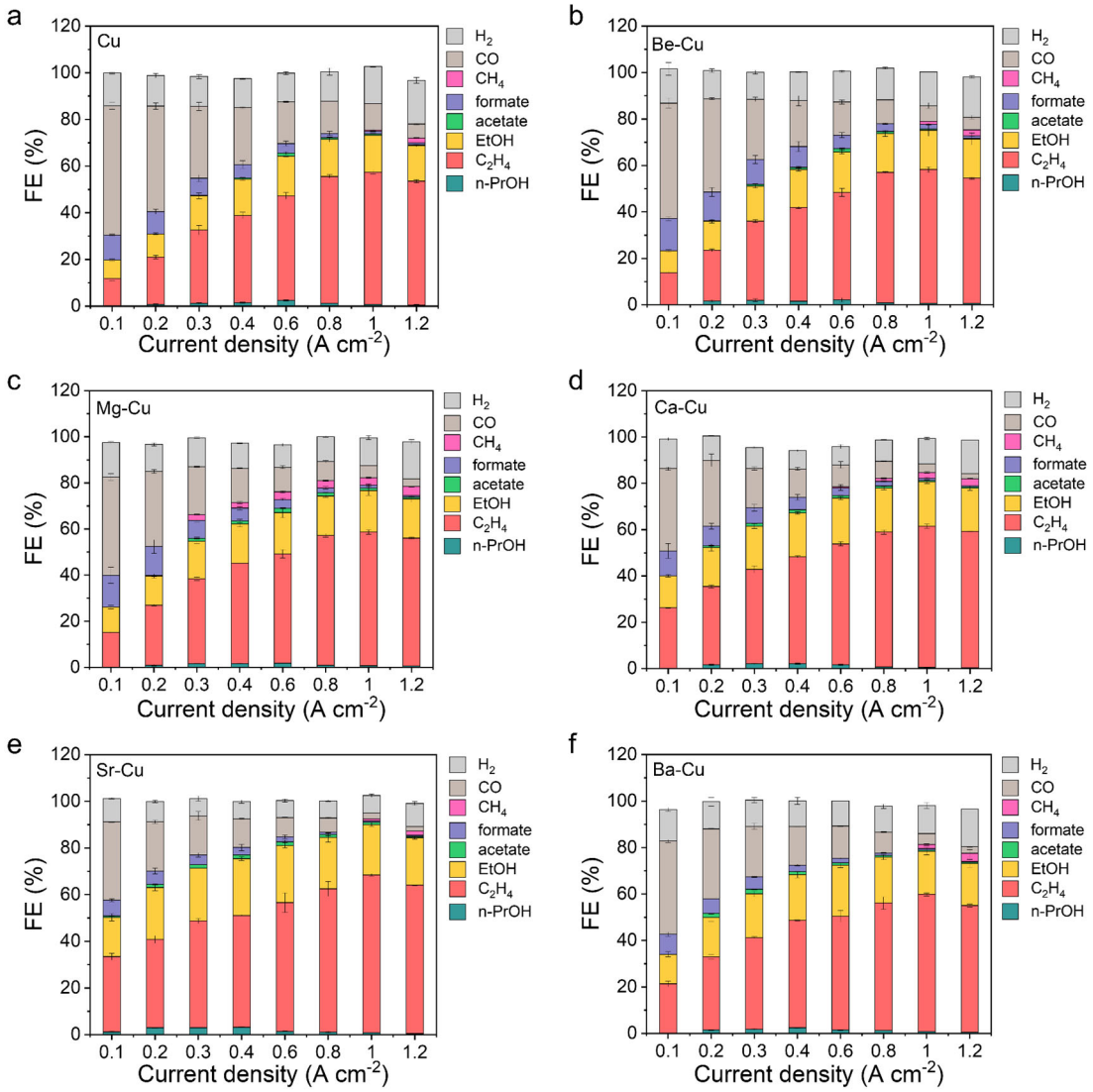

Supplementary Fig. 12 | Faradaic efficiencies of different products over the X-Cu catalysts under the applied current density ranging from 0.1 to 1.2 A cm^{-2} in 1 M KOH. a, Cu. **b,** Be-Cu. **c,** Mg-Cu. **d,** Ca-Cu. **e,** Sr-Cu. **f,** Ba-Cu. The error bars represent the standard deviation of three independent electrocatalytic experiments.

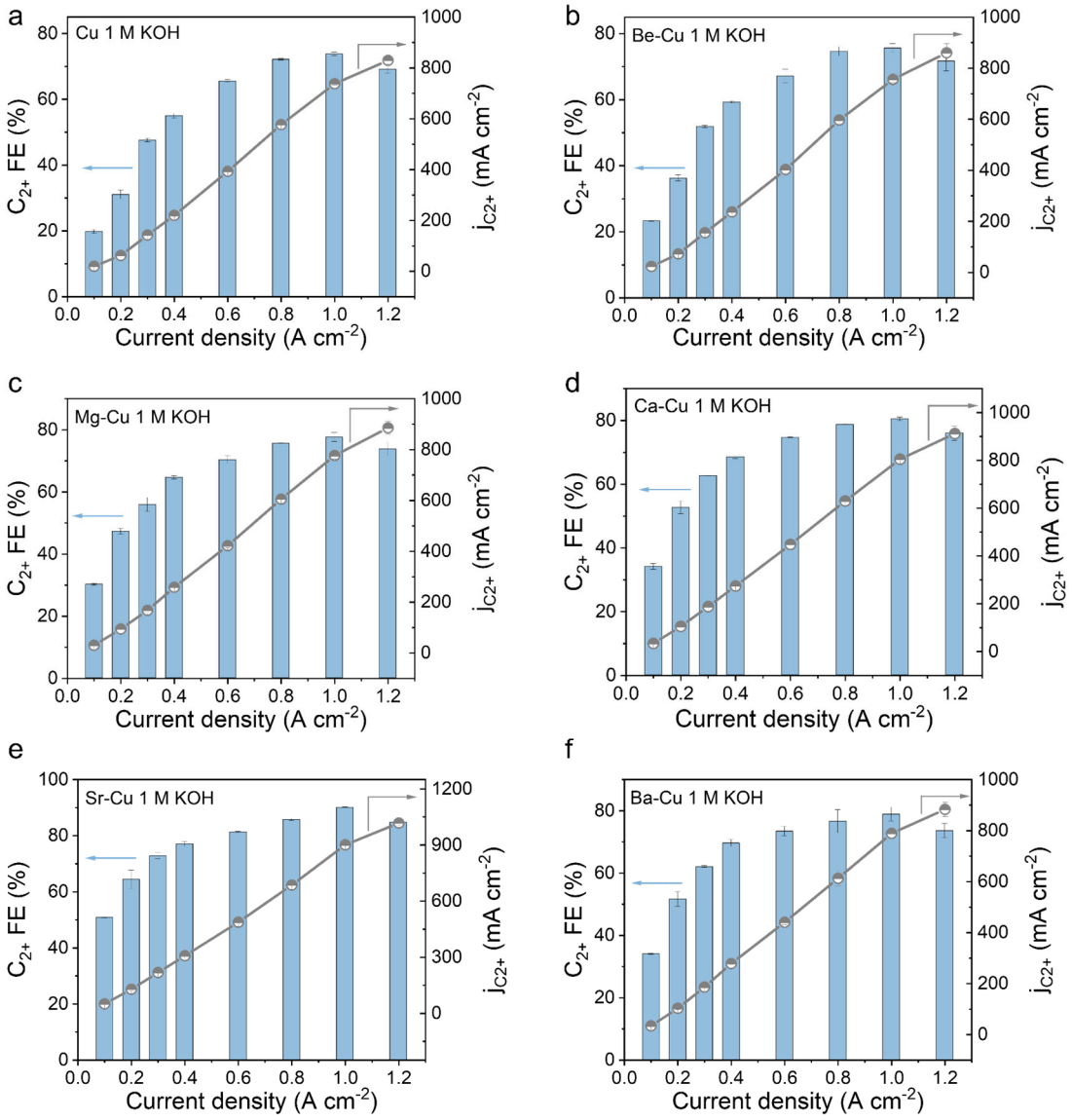

Supplementary Fig. 13 | C_{2+} Faradaic efficiencies and partial current densities over X-Cu catalysts under applied current density ranging from 0.1 to 1.2 A cm^{-2} in 1 M KOH. a, Cu. **b,** Be-Cu. **c,** Mg-Cu. **d,** Ca-Cu. **e,** Sr-Cu. **f,** Ba-Cu. The error bars represent the standard deviation of three independent electrocatalytic experiments.

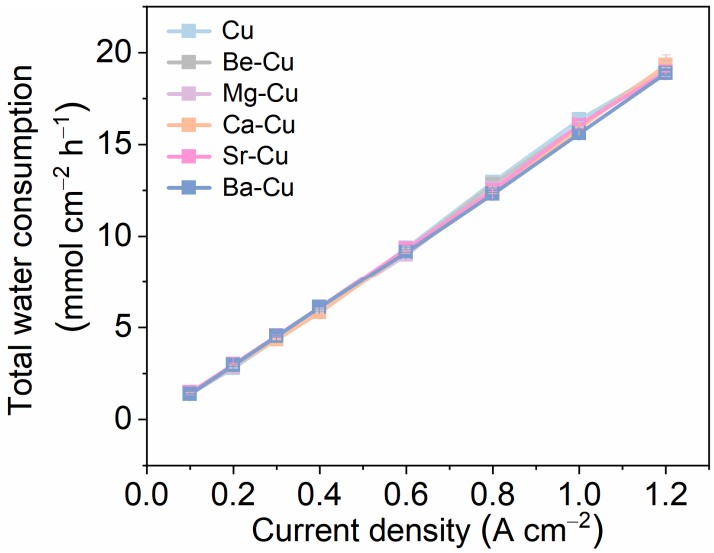

Supplementary Fig. 14 | The total water consumption of X-Cu catalysts at various current densities.

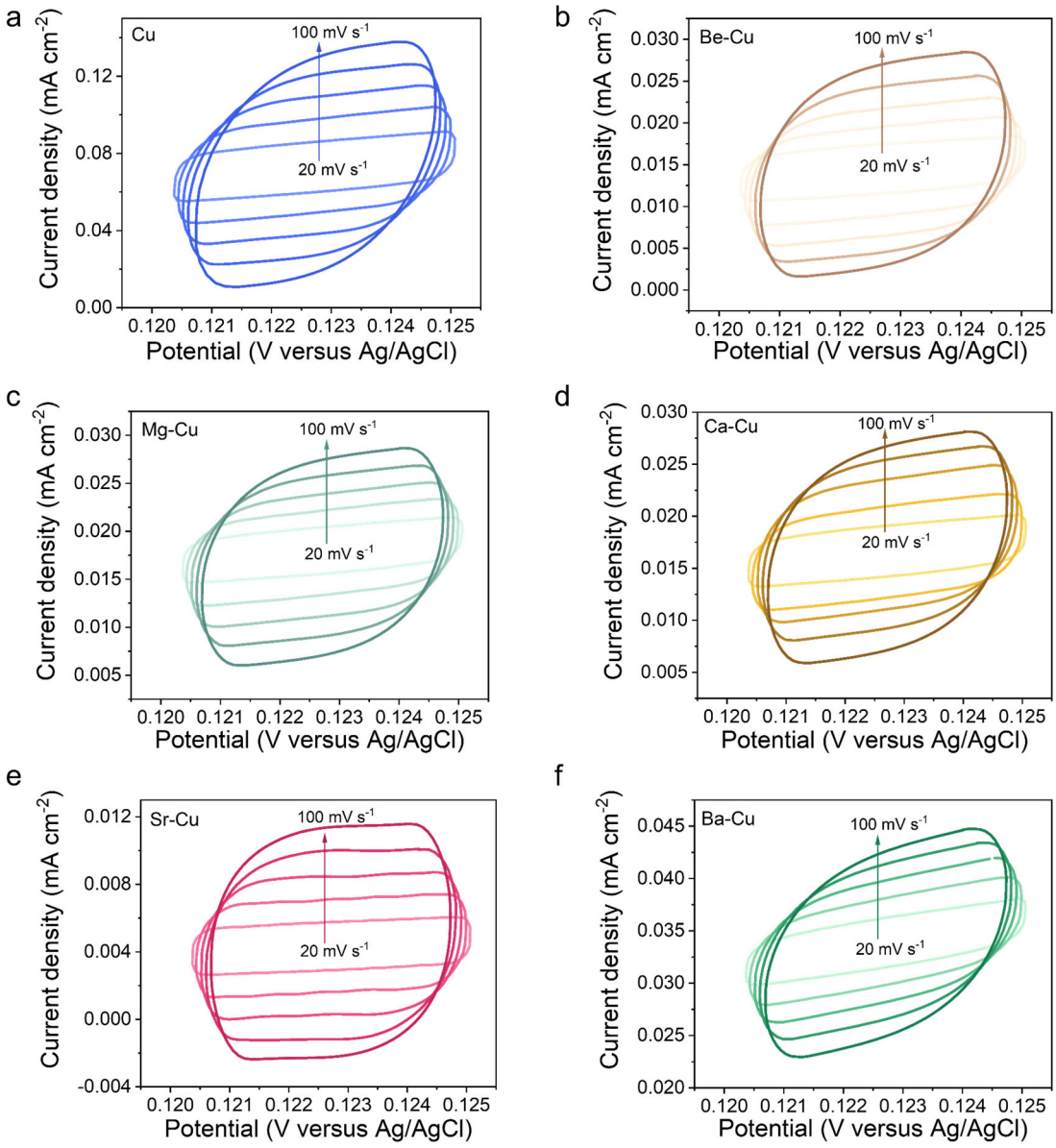

Supplementary Fig. 15 | Electrochemical cyclic voltammetry of X-Cu in the non-Faradaic region. a, Cu. **b,** Be-Cu. **c,** Mg-Cu. **d,** Ca-Cu. **e,** Sr-Cu. **f,** Ba-Cu. In the measurement, the potential window for cyclic voltametric stripping was 0.120 to 0.125 V versus Ag/AgCl in an Ar-saturated 1 M KOH electrolyte at scan rates of 20, 40, 60, 80, and 100 mV s^{-1}.

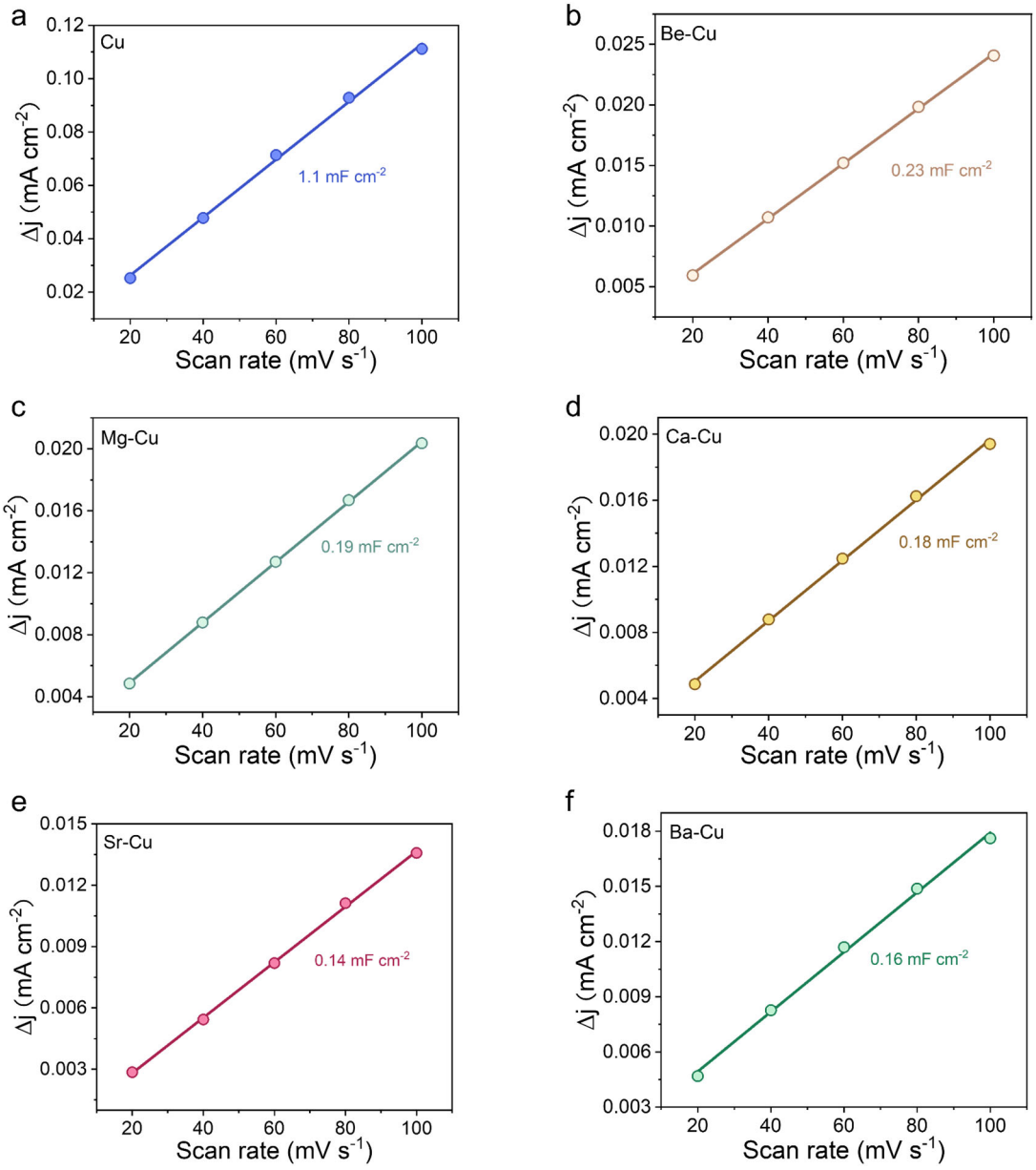

Supplementary Fig. 16 | Double-layer capacitance (C_{dl}) of X-Cu catalysts. a, Cu. **b,** Be-Cu. **c,** Mg-Cu. **d,** Ca-Cu. **e,** Sr-Cu. **f,** Ba-Cu. The C_{dl} values were determined by measuring the capacitive current density associated with double-layer charging from the scan-rate dependence of cyclic voltametric stripping. The C_{dl} values were estimated by plotting $\Delta j = (j_a - j_c)$ at 0.1225 V (where j_c and j_a are the cathodic and anodic current densities, respectively) versus the Ag/AgCl reference against the scan rate.

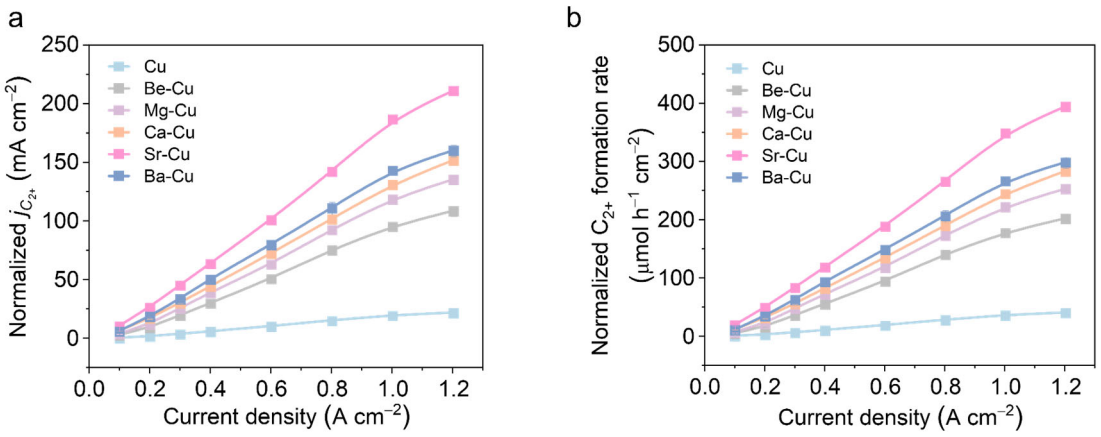

Supplementary Fig. 17 | ECSA-normalized C_{2+} formation performance of X-Cu catalysts at different current densities in 1.0 M KOH. a, ECSA-normalized C_{2+} partial current densities of X-Cu catalysts at various current densities in 1.0 M KOH. **b,** ECSA-normalized C_{2+} formation rates of the X-Cu catalysts at different applied current densities in 1.0 M KOH. The experiments in each case were performed in triplicate, and the results are shown as mean ± standard deviation.

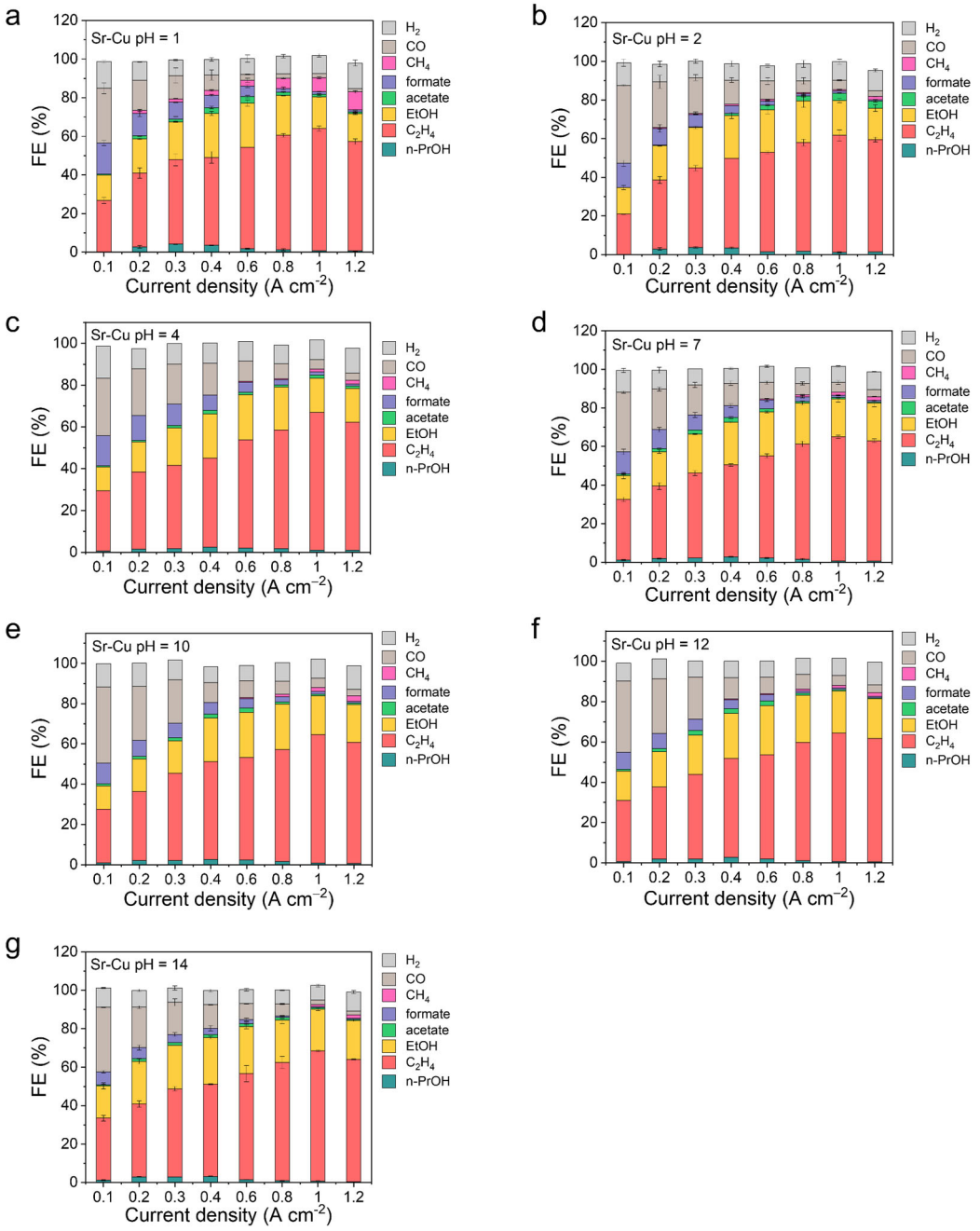

Supplementary Fig. 18 | Faradaic efficiencies of CO_2RR products over the Sr-Cu catalyst at different pH values and different applied current densities. a, pH = 1; **b,** pH = 2; **c,** pH = 4; **d,** pH = 7; **e,** pH = 10; **f,** pH = 12; **g,** pH = 14. The experiments in each case were performed in triplicate, and the results are shown as mean ± standard deviation.

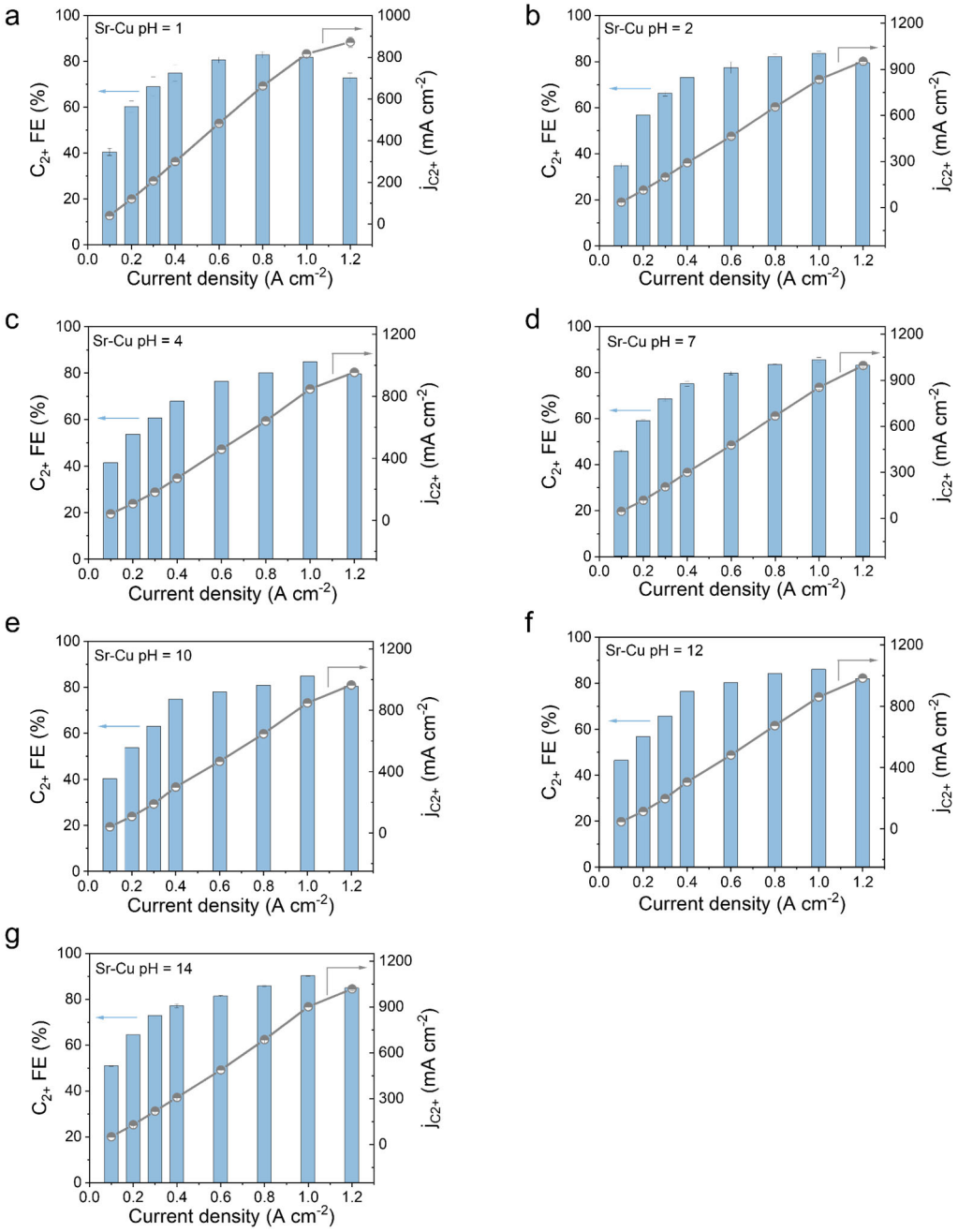

Supplementary Fig. 19 | C_{2+} Faradaic efficiencies and partial current densities over the Sr-Cu catalyst at different pH values under different applied current densities. a, pH = 1; **b,** pH = 2; **c,** pH = 4; **d,** pH = 7; **e,** pH = 10; **f,** pH = 12; **g,** pH = 14. The error bars represent the standard deviation of three independent electrocatalytic experiments.

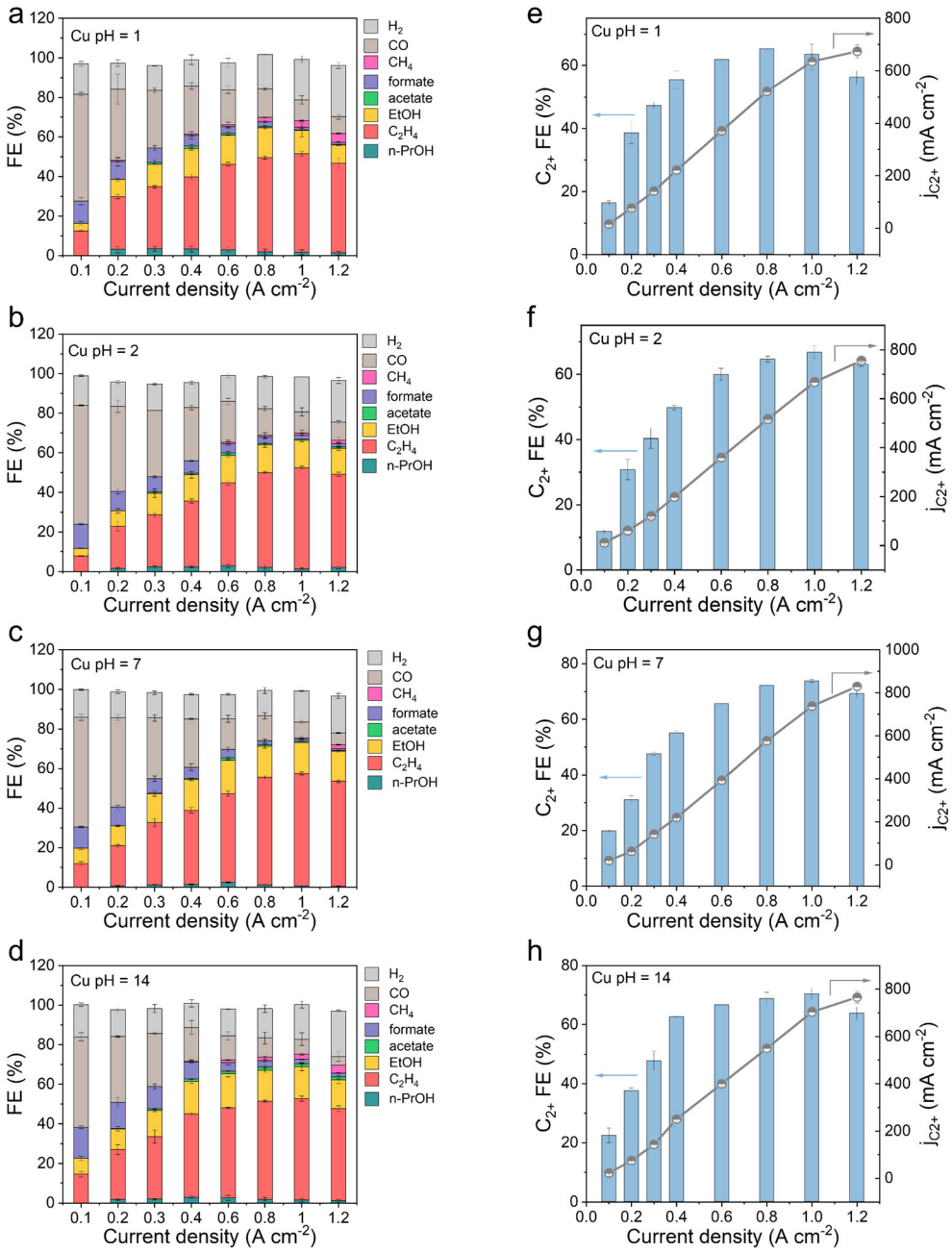

Supplementary Fig. 20 | Faradaic efficiency of different products and corresponding C_{2+} FE and j_{C2+} over Cu catalyst at various current densities in different pH electrolytes. a, e, pH = 1. **b, f,** pH = 2. **c, g,** pH = 7. **d, h,** pH = 14. The error bars represent the standard deviation of three independent electrocatalytic experiments.

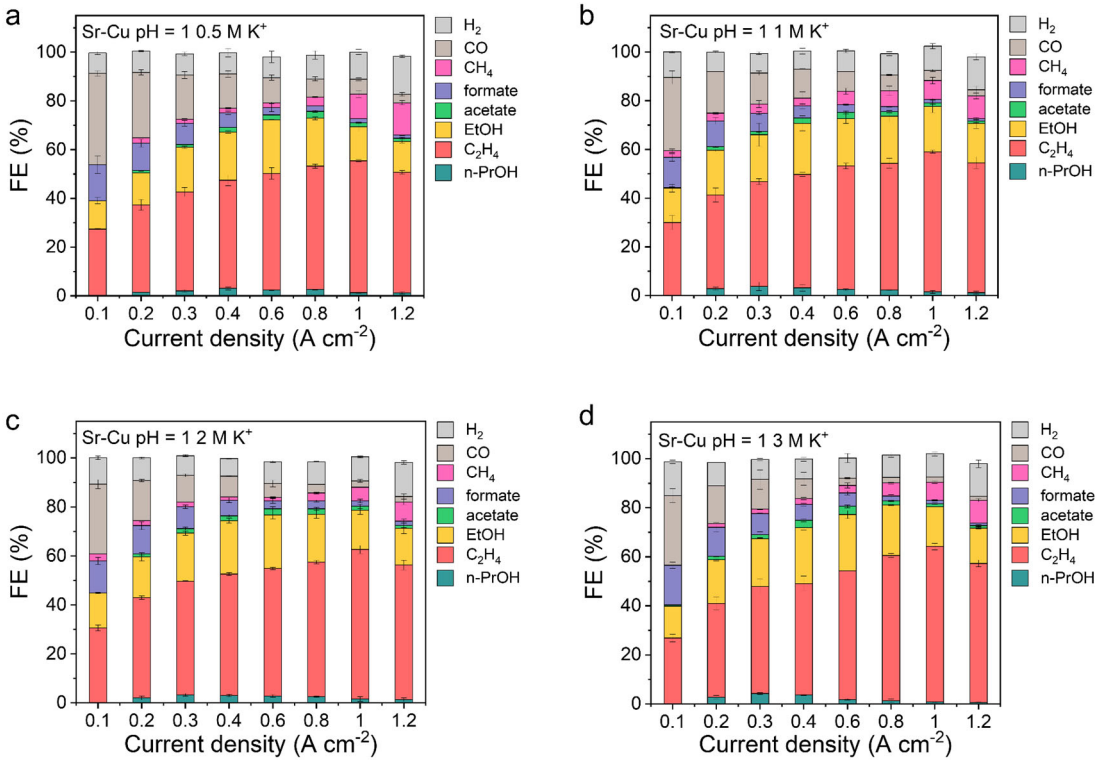

Supplementary Fig. 21 | Faradaic efficiencies of CO_2RR products over the Sr-Cu catalyst in electrolytes with different K^+ concentrations at pH 1. a, 0.5 M K^+; **b,** 1 M K^+; **c,** 2 M K^+; **d,** 3 M K^+. The experiments in each case were performed in triplicate, and the results are shown as mean ± standard deviation.

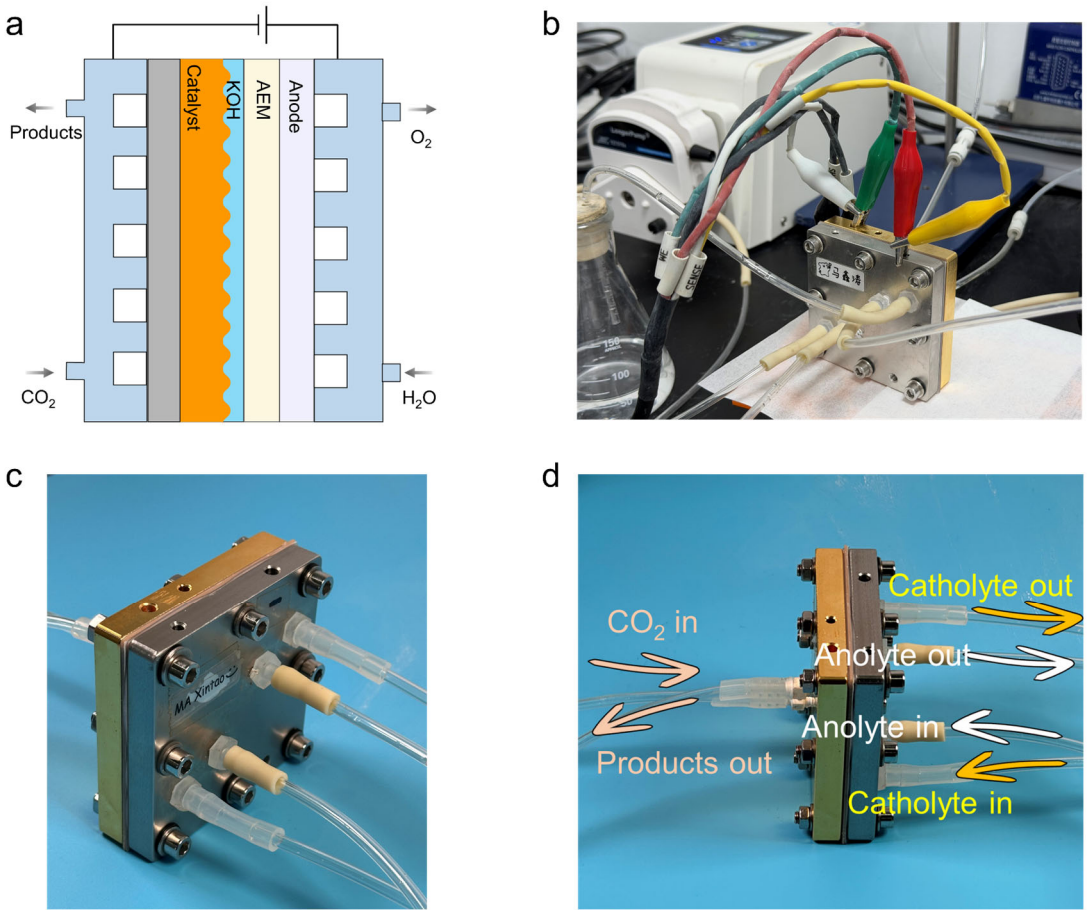

Supplementary Fig. 22 | Schematic illustration and photographs of the microchannel device. a, Schematic illustration of the microchannel. **b–d,** Photographs of the microchannel device. The microchannel device provides a compact full-cell configuration that enables efficient reactant transport, rapid product removal, and a stable gas-liquid-solid interface for high-rate CO_2RR. Its confined flow-channel geometry helps mitigate mass-transfer limitations and maintain stable operation at high current densities.

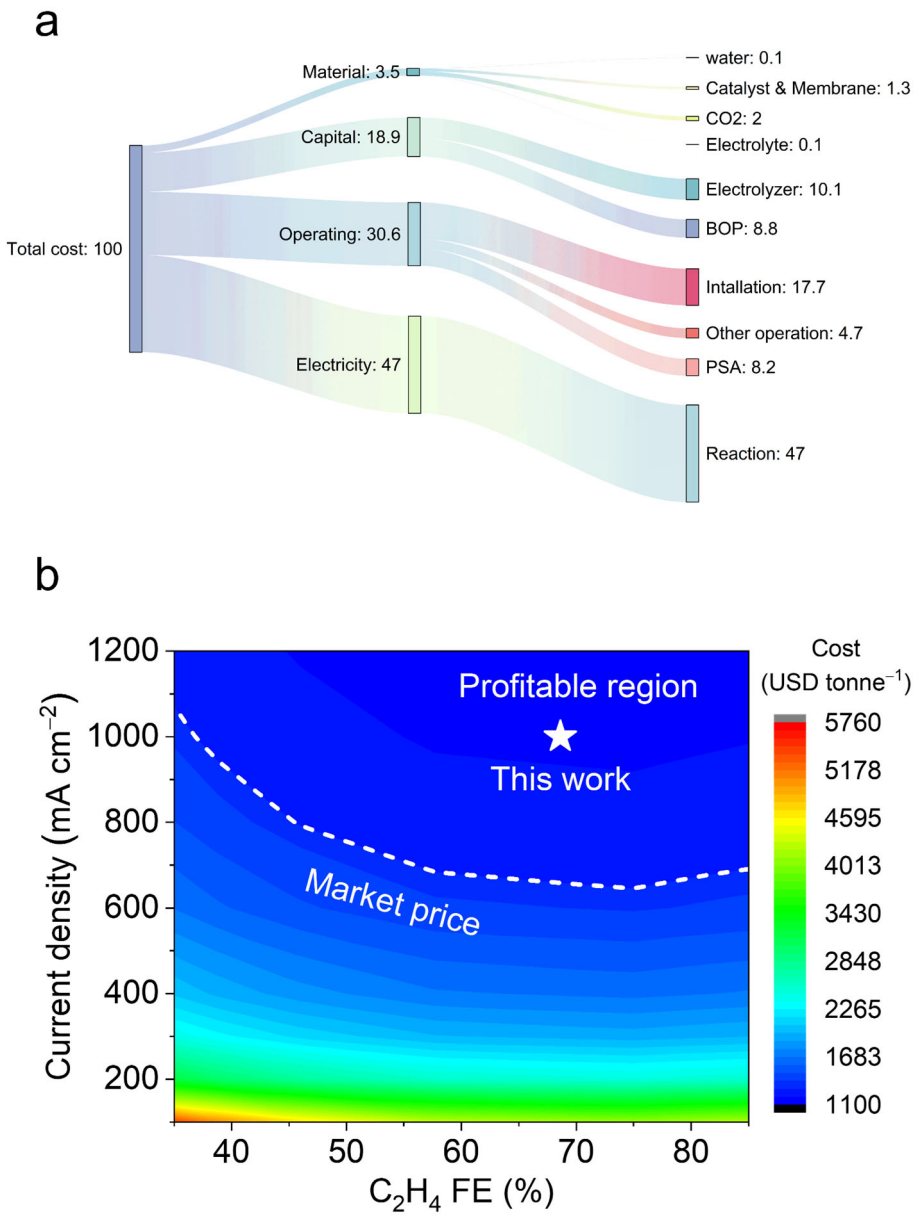

Supplementary Fig. 23 | Techno-economic analysis of Sr-Cu microchannel system. **a,** The subdivided cost of the entire process for CO_2RR-to-ethylene at a current density of 1.0 A cm^{-2} and FE of 68.6% at the given electricity price of USD 0.01 per kWh. **b,** The cost analysis for the generation of ethylene from CO_2RR with the change in current density and FE.

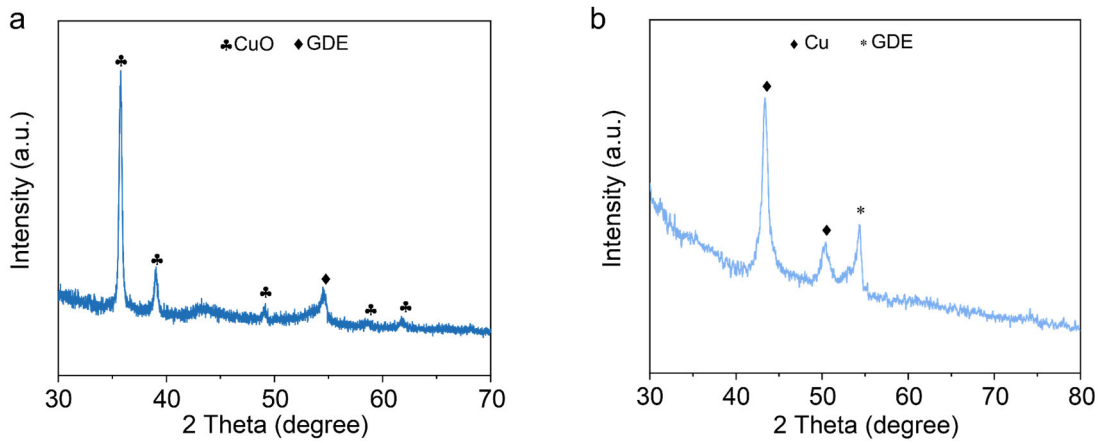

Supplementary Fig. 24 | XRD patterns of CuO precursor and Cu catalyst deposited on GDE. a, CuO before reaction. **b,** CuO after reaction. Before the CO_2RR, the catalyst loaded on GDE exhibits diffraction patterns characteristic of the CuO phase. After the CO_2RR, the XRD pattern reveals the complete disappearance of CuO phase, and the emergence of peaks assigned to metallic Cu.

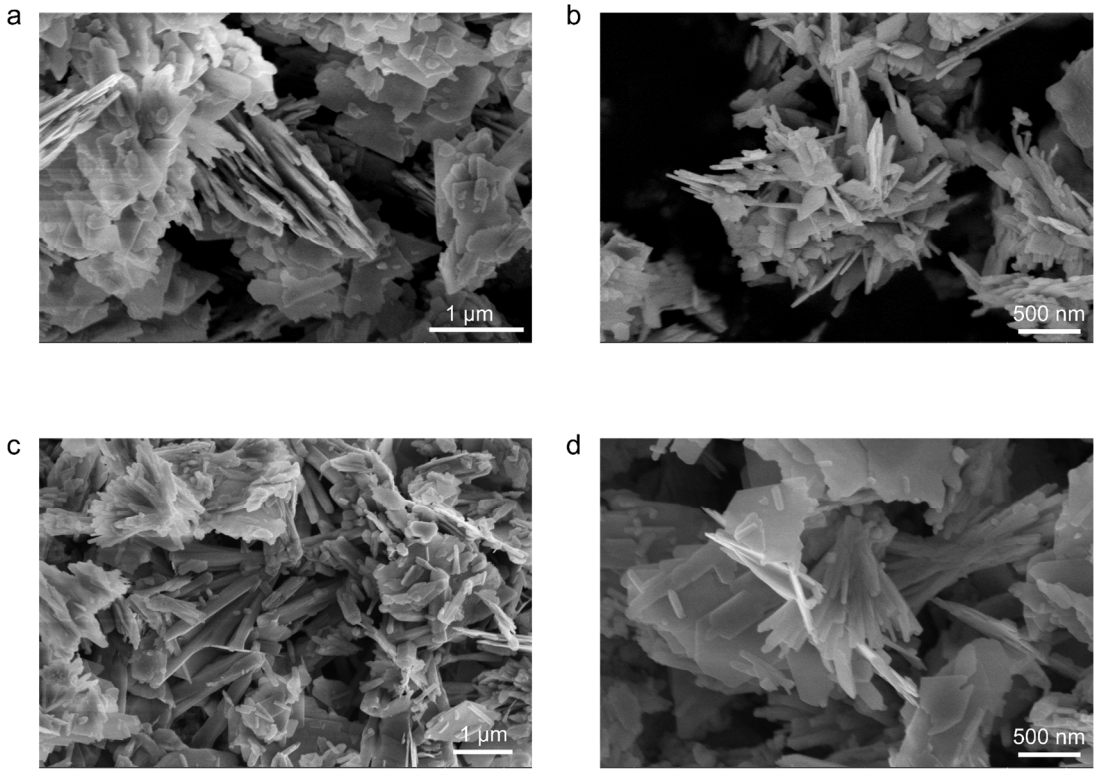

Supplementary Fig. 25 | SEM images of Cu and Sr-Cu catalyst at different magnification. a, b, Cu catalyst. **c, d,** Sr-Cu catalyst.

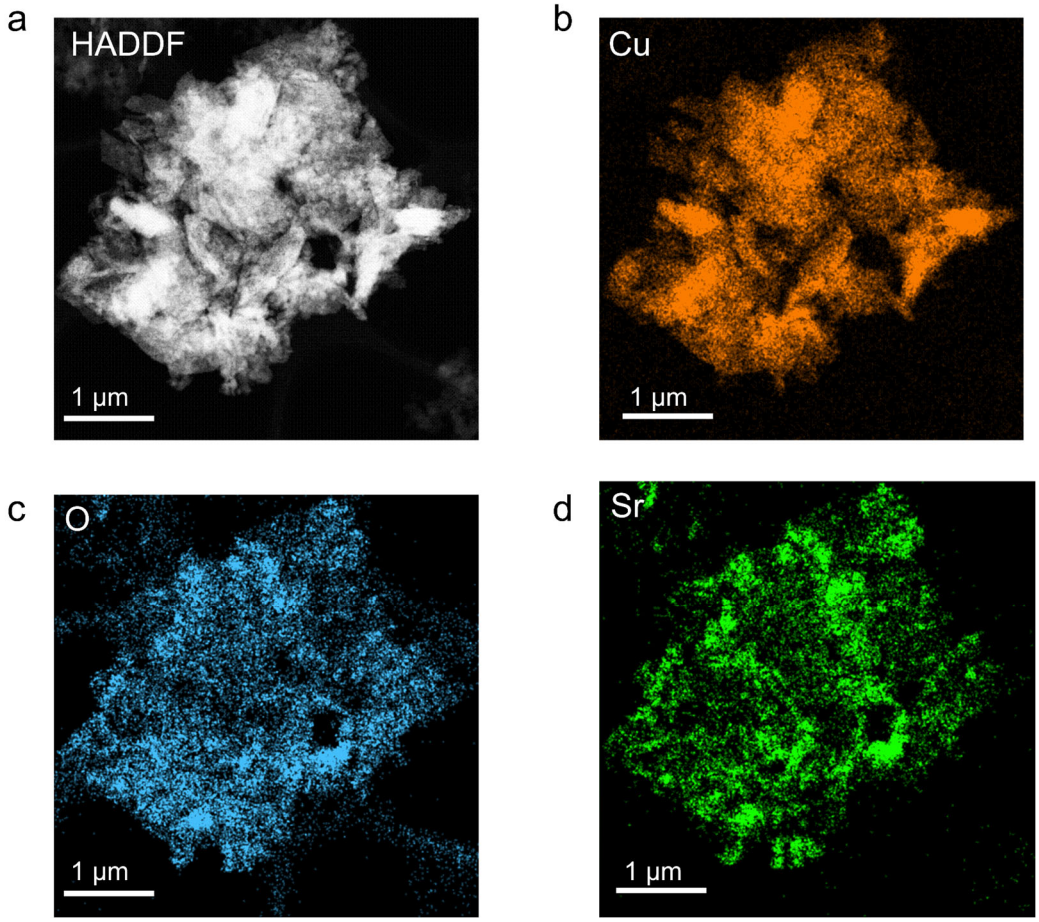

Supplementary Fig. 26 | HAADF-STEM and corresponding EDS elemental mapping images of Sr-Cu catalyst. a, HADDF-STEM image of Sr-Cu catalyst. **b–d,** Corresponding EDS elemental mappings of Cu **(b)**, O **(c)**, and Sr **(d)**.

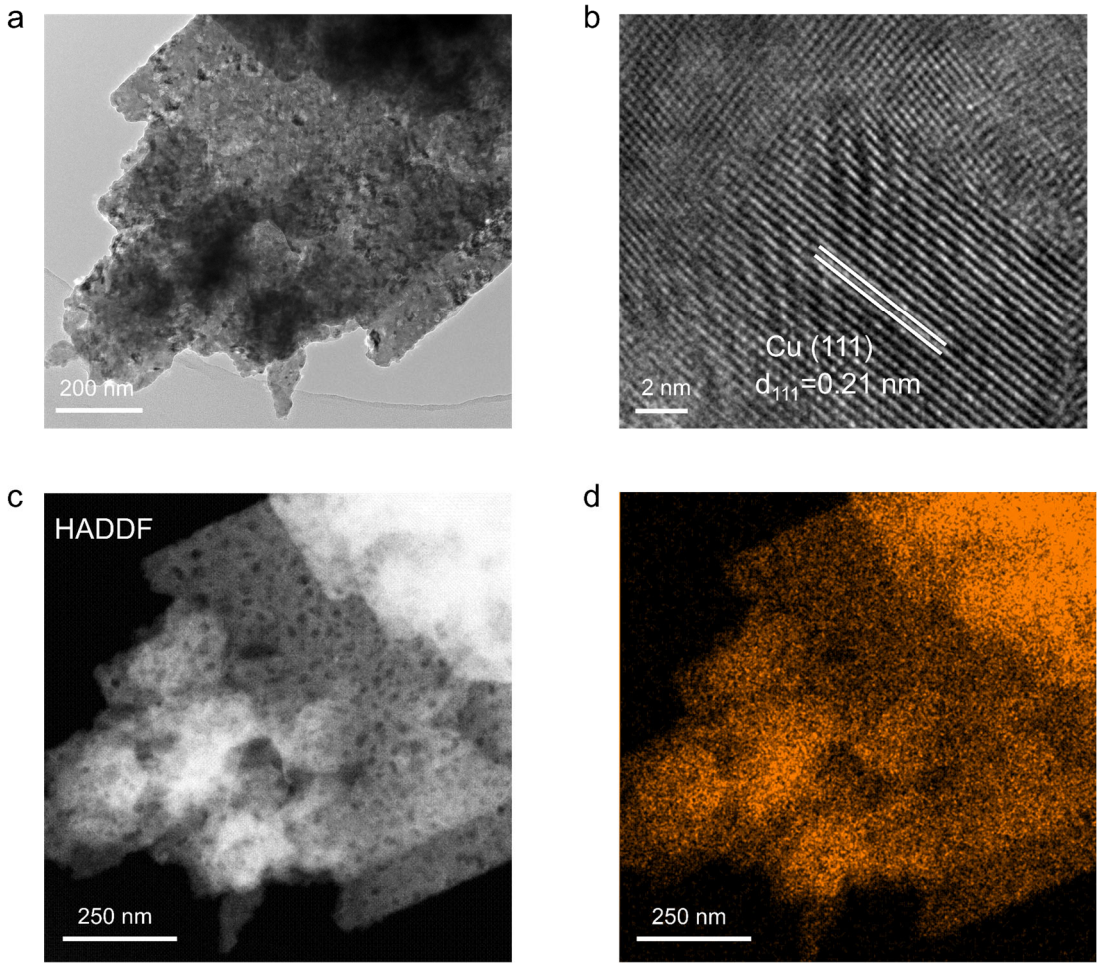

Supplementary Fig. 27 | HRTEM and HAADF-STEM and corresponding EDS elemental mapping images of Cu catalyst. a, TEM image of Cu catalyst. **b,** HRTEM image of Cu catalyst showing the lattice fringes. **c,** HADDF-STEM image of Cu catalyst. **d,** Corresponding EDS elemental mapping of Cu.

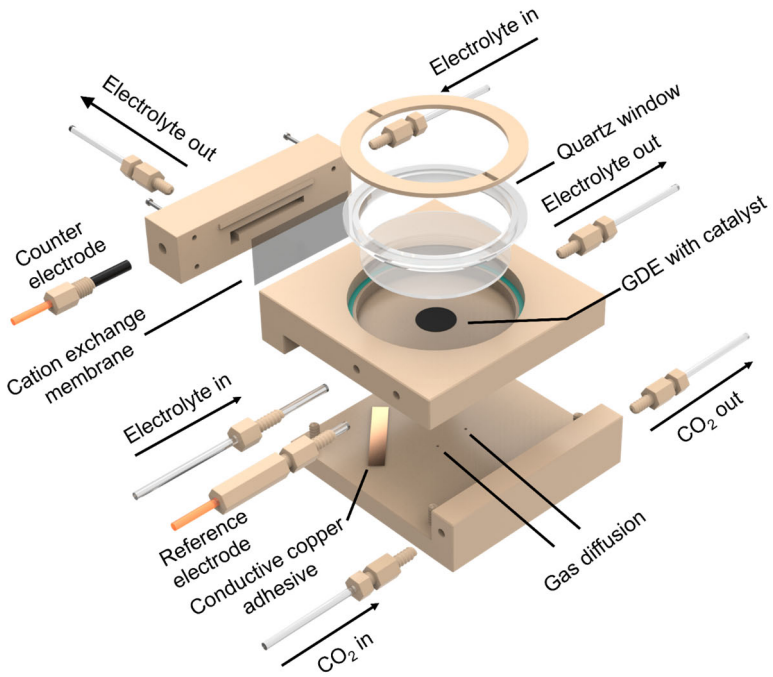

Supplementary Fig. 28 | Schematic setup of the modified flow cell for the *operando* Raman measurements.

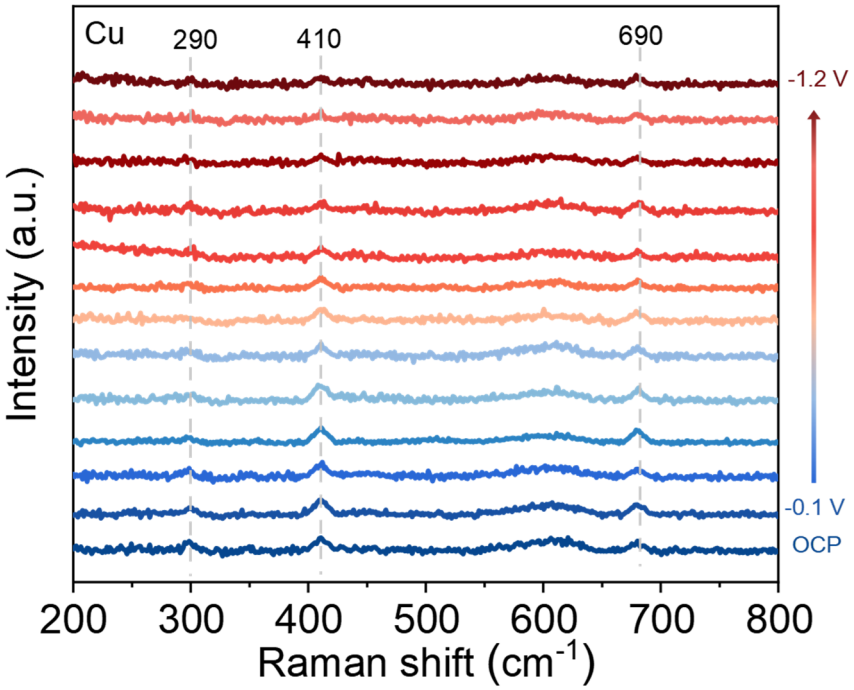

Supplementary Fig. 29 | *Operando* Raman spectra of Cu catalyst at various applied potentials.

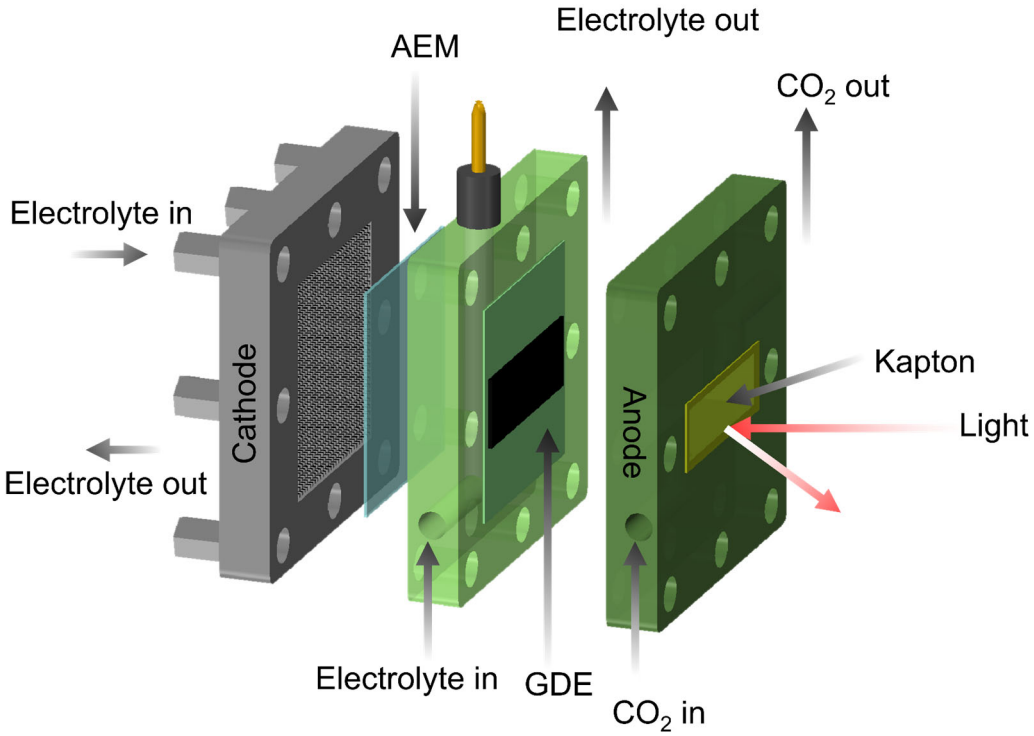

Supplementary Fig. 30 | Schematic setup of the modified flow cell for the *operando* XAS measurements.

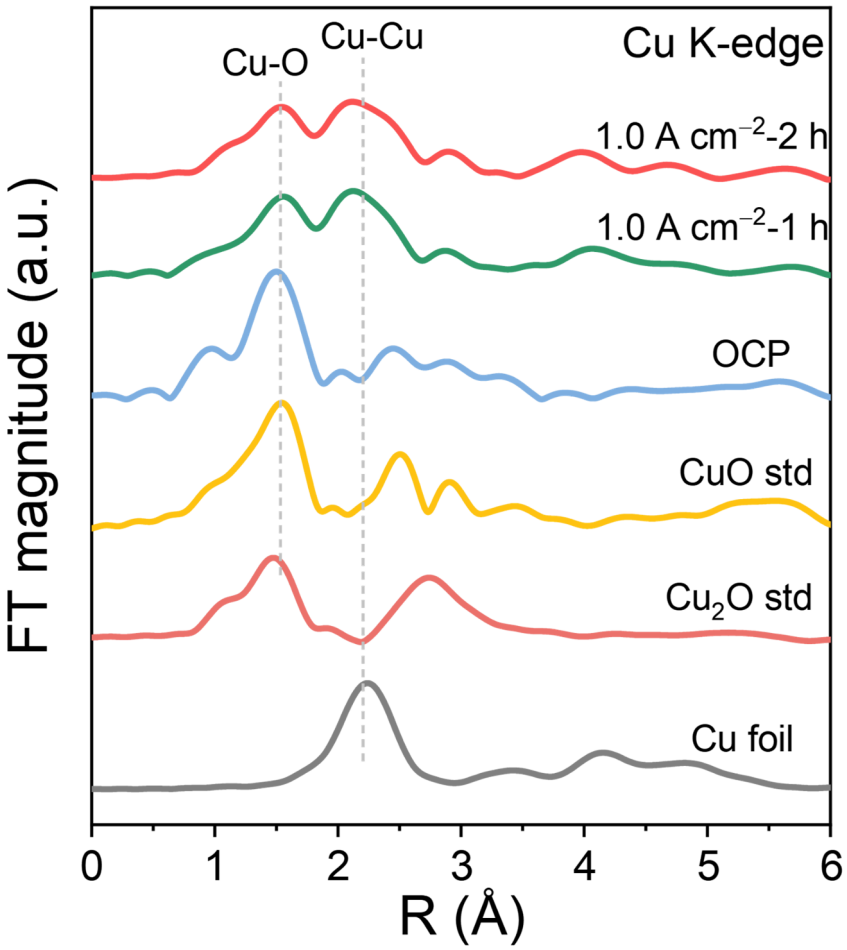

Supplementary Fig. 31 | R-space spectra of *operando* Cu K-edge EXAFS for Sr-Cu catalyst under different testing conditions.

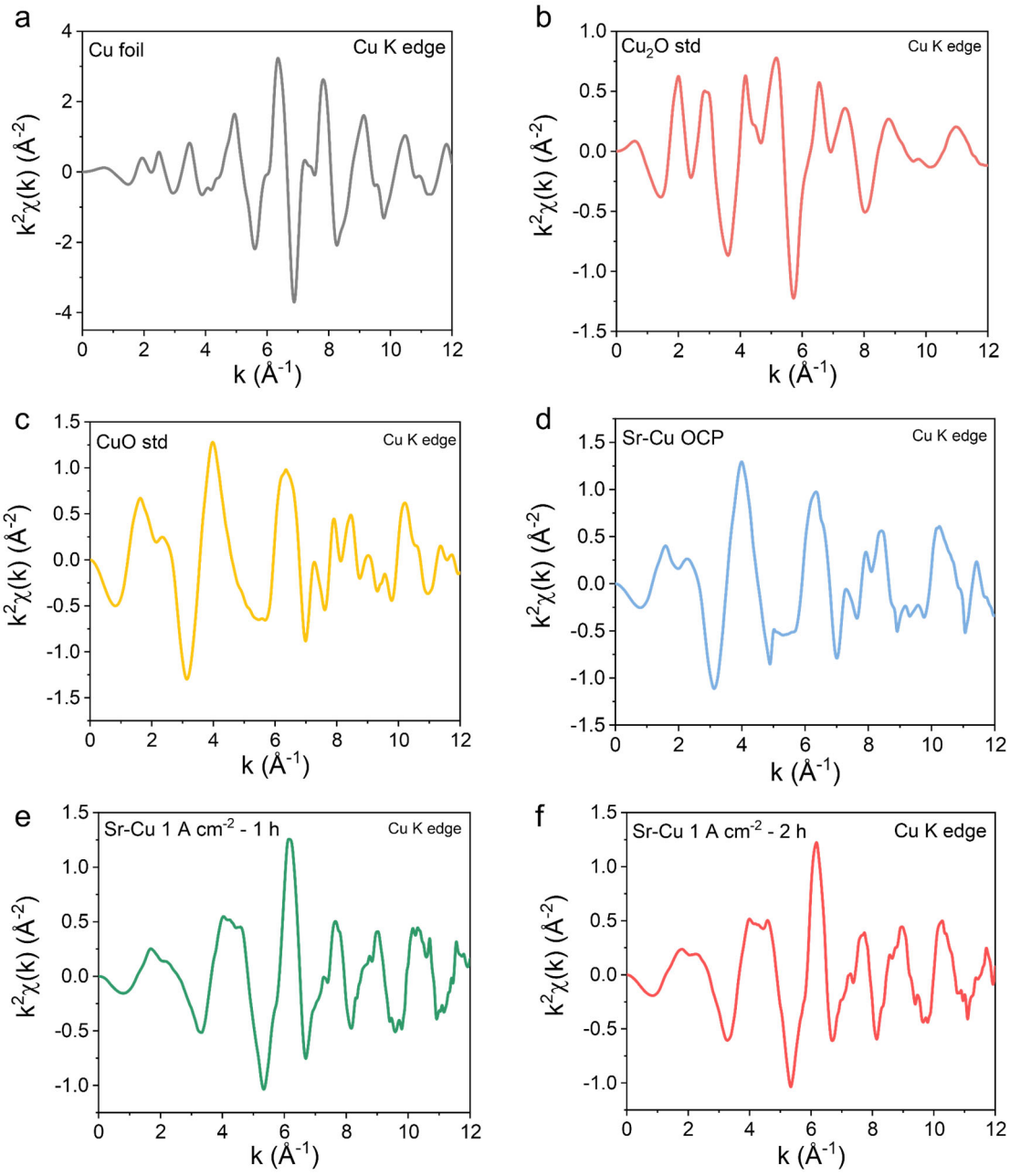

Supplementary Fig. 32 | The k-space results on *operando* Cu K-edge XANES of Sr-Cu catalysts at different testing conditions and the references. a, Cu foil. **b,** Cu_2O std. **c,** CuO std. **d,** Sr-Cu at OCP. **e,** Sr-Cu at 1 A cm^{-2} for 1 h. **f,** Sr-Cu at 1 A cm^{-2} for 2 h.

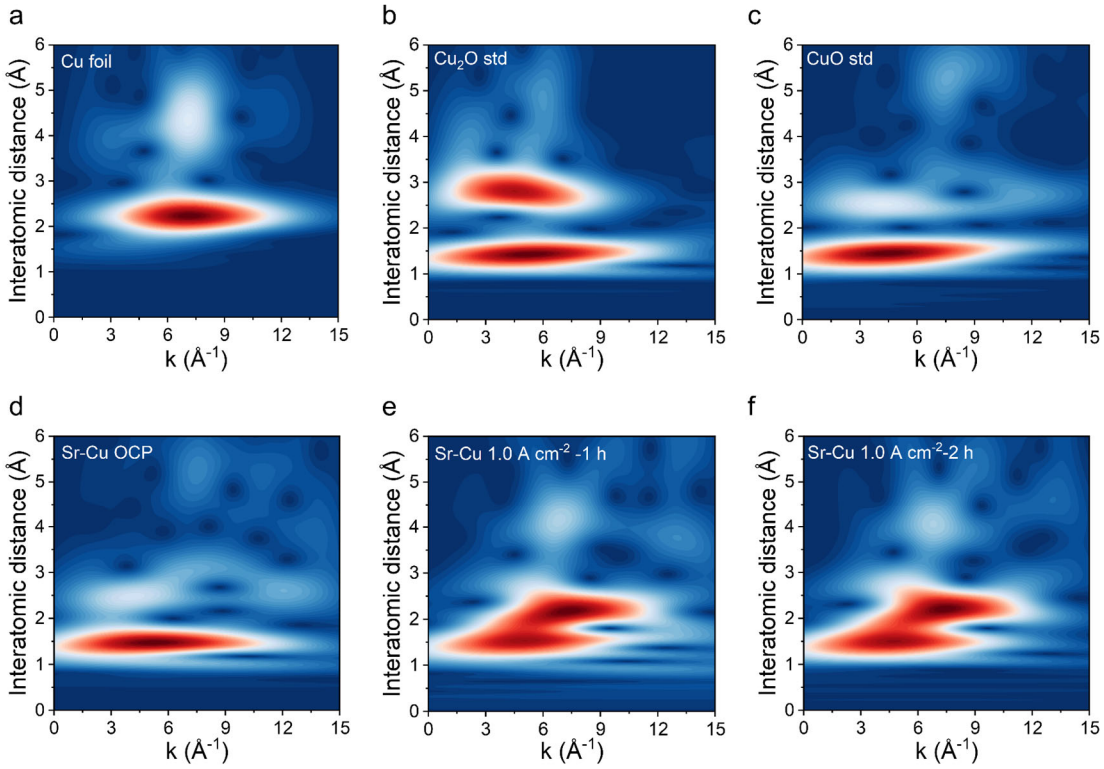

Supplementary Fig. 33 | Wavelet transform (WT) of the k^2-weight *operando* EXAFS data for the Sr-Cu catalyst under different testing conditions. a, Cu foil. **b,** Cu_2O std. **c,** CuO std. **d,** At open circuit potential. **e,** electrolysis at 1.0 A cm^{-2} for 1 h. **f,** electrolysis at 1.0 A cm^{-2} for 2 h. The WT analysis results demonstrated that the coexistence of Cu–O and Cu–Cu bonds in the Sr-Cu catalyst during CO_2RR.

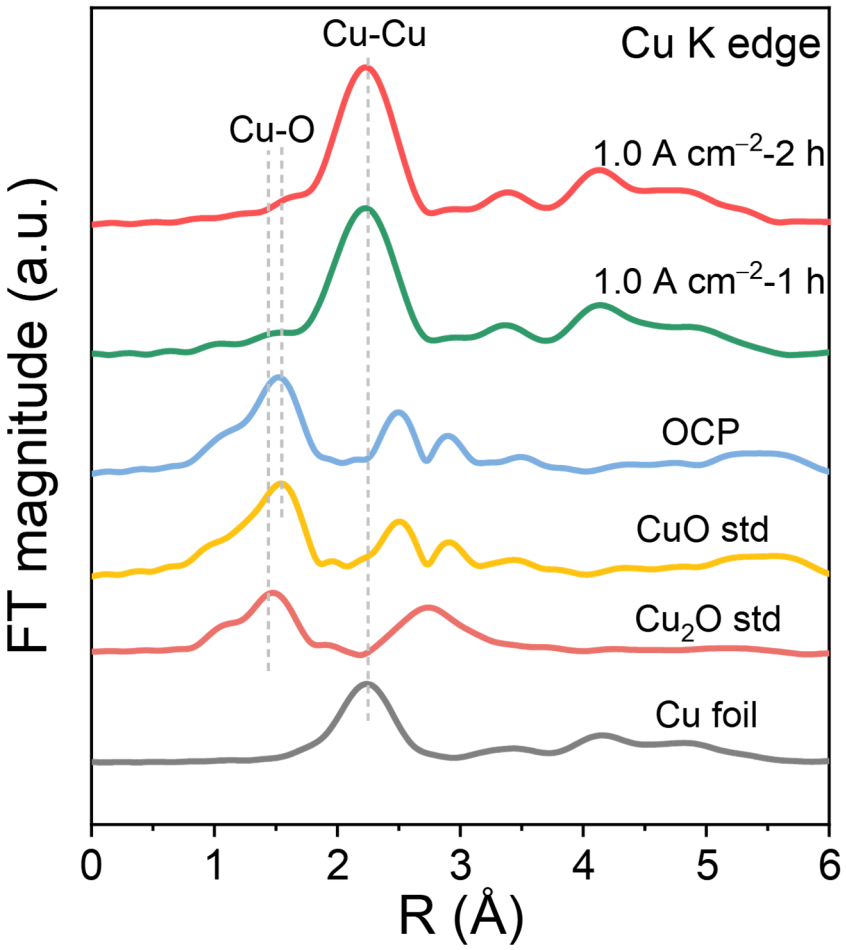

Supplementary Fig. 34 | R-space spectra of Cu K-edge EXAFS for Cu catalyst under different testing conditions.

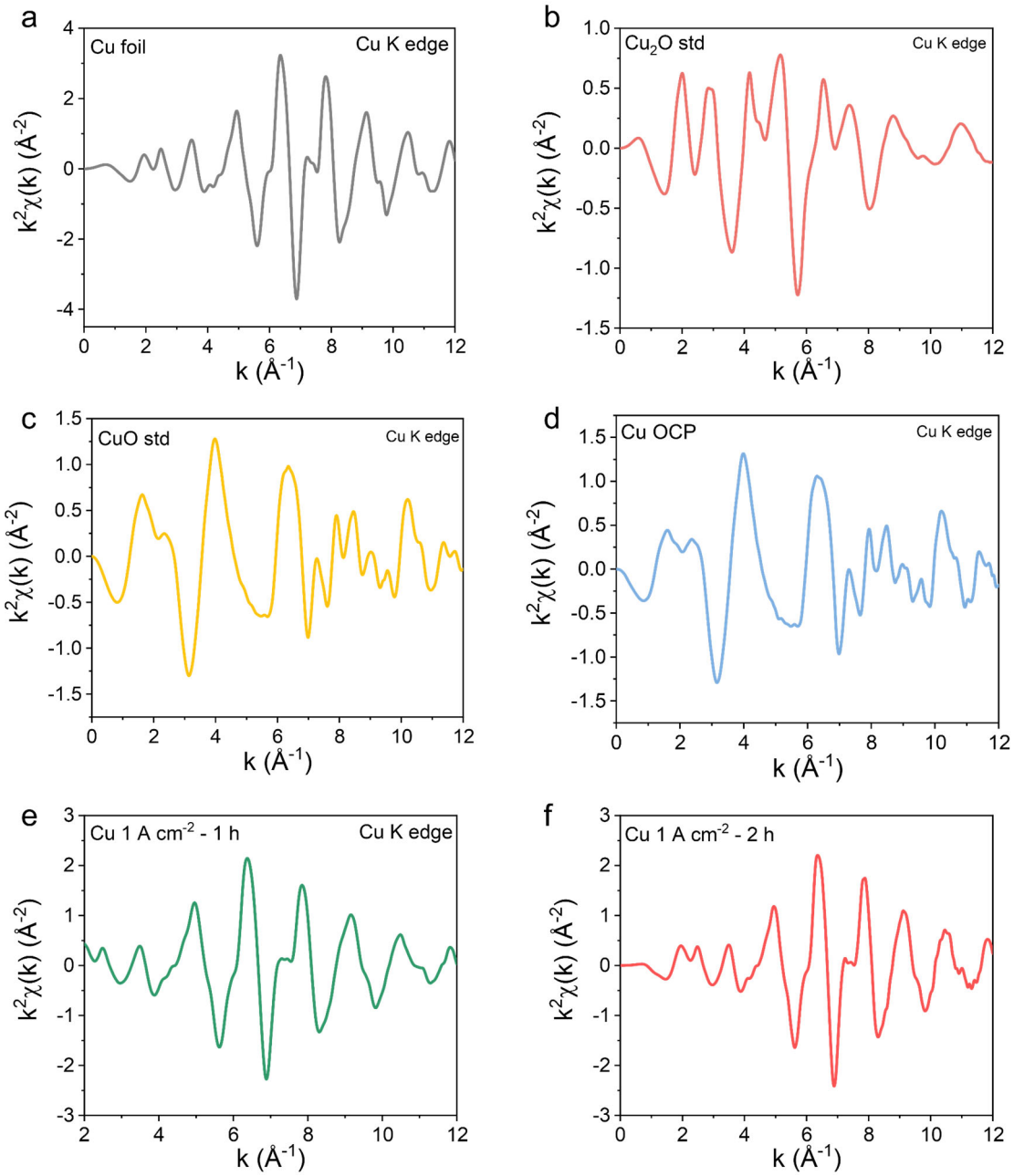

Supplementary Fig. 35 | The k-space results on in situ Cu K-edge XANES of Cu catalysts at different testing conditions and the references. a, Cu foil. **b,** Cu_2O std. **c,** CuO std. **d,** Cu at OCP. **e,** Cu at 1 A cm^{-2} for 1 h. **f,** Cu at 1 A cm^{-2} for 2 h.

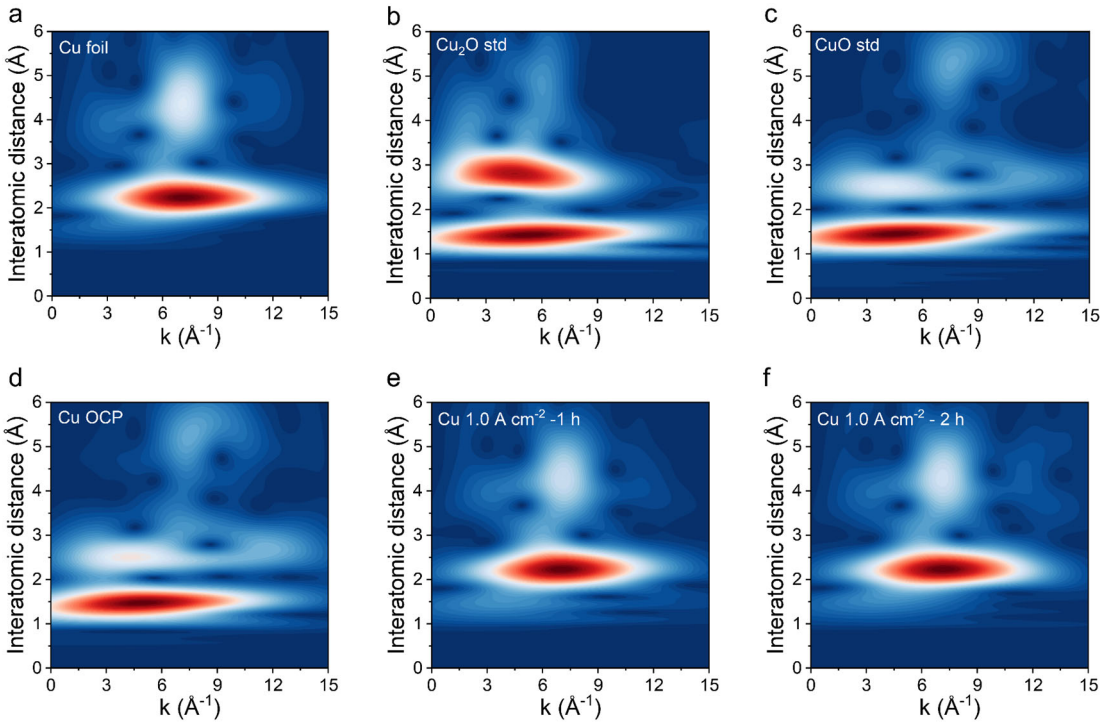

Supplementary Fig. 36 | Wavelet transform (WT) of the k^2-weight *operando* EXAFS data for the Cu catalyst under different testing conditions. a, Cu foil. **b,** Cu_2O std. **c,** CuO std. **d,** At open circuit potential. **e,** electrolysis at 1.0 A cm^{-2} for 1 h. **f,** electrolysis at 1.0 A cm^{-2} for 2 h. The WT analysis results demonstrated that only the Cu–Cu bond in the Cu catalyst during CO_2RR.

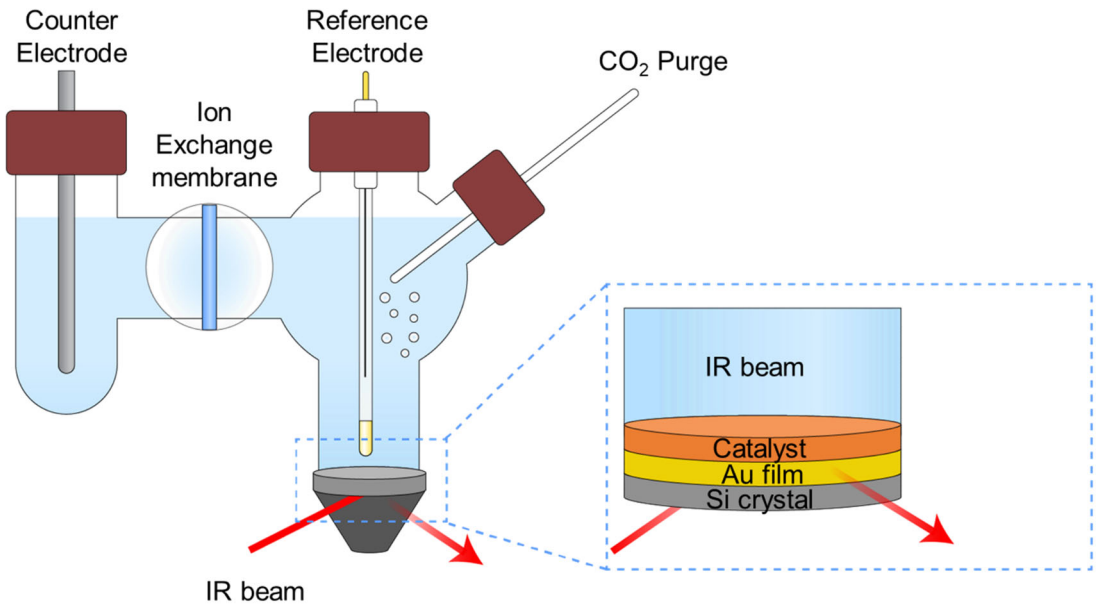

Supplementary Fig. 37 | Schematic setup of the in situ electrochemical attenuated total reflectance-Fourier transform infrared (ATR-FTIR).

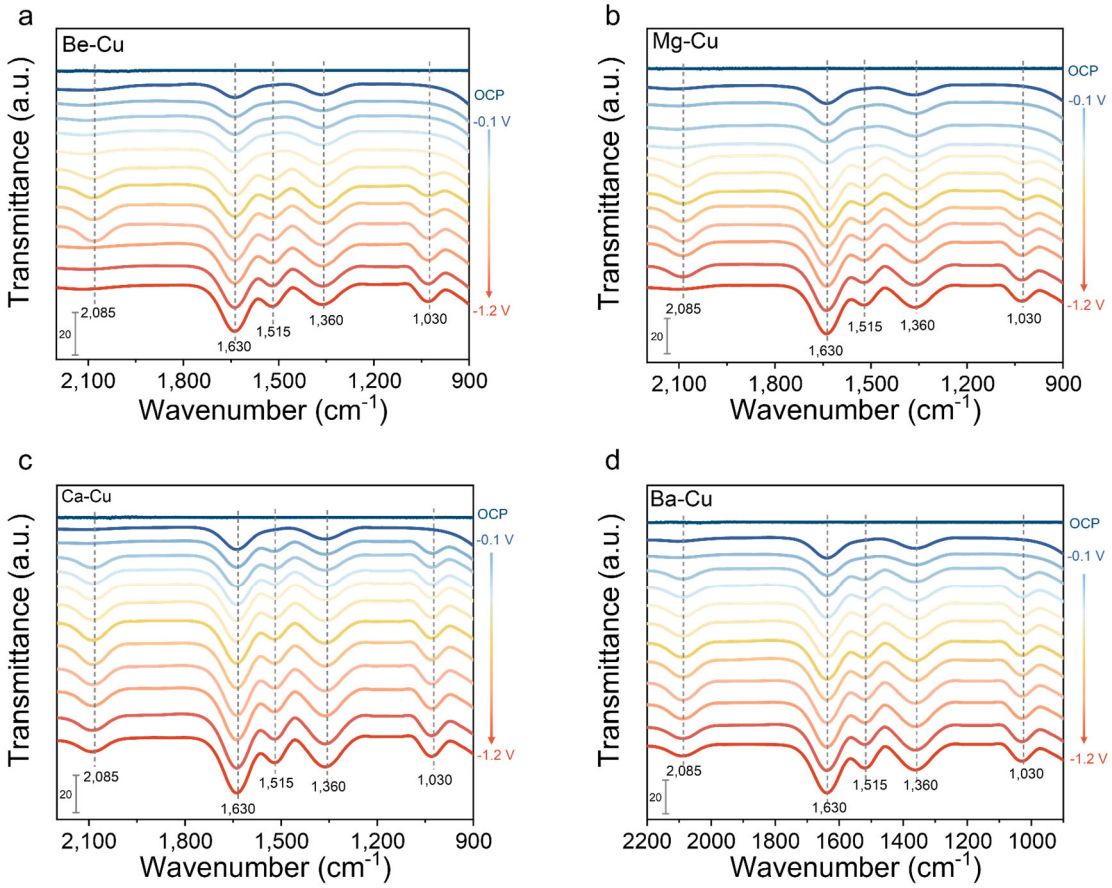

Supplementary Fig. 38 | In situ ATR-FTIR spectra recorded at different applied potentials over X-Cu catalysts. a, Be-Cu. **b,** Mg-Cu. **c,** Ca-Cu. **d,** Ba-Cu.

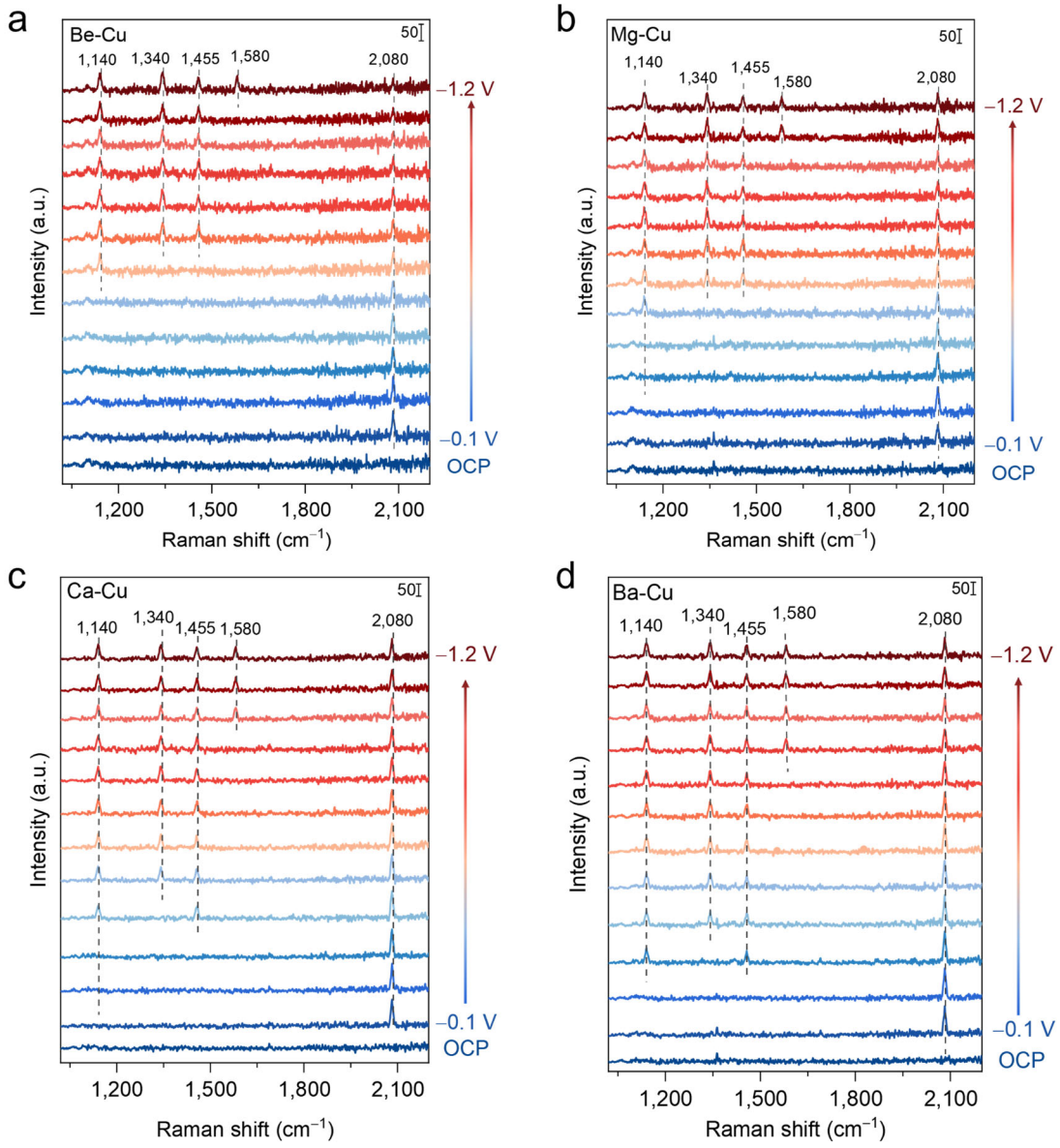

Supplementary Fig. 39 | *Operando* Raman spectra recorded at different potentials over X-Cu catalysts. a, Be-Cu. **b,** Mg-Cu. **c,** Ca-Cu. **d,** Ba-Cu.

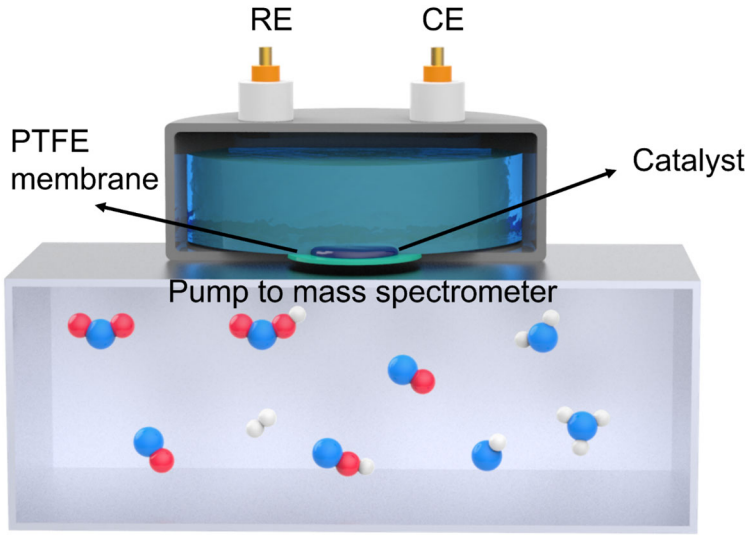

Supplementary Fig. 40 | Schematic setup of the in situ differential electrochemical mass spectrometry (DEMS).

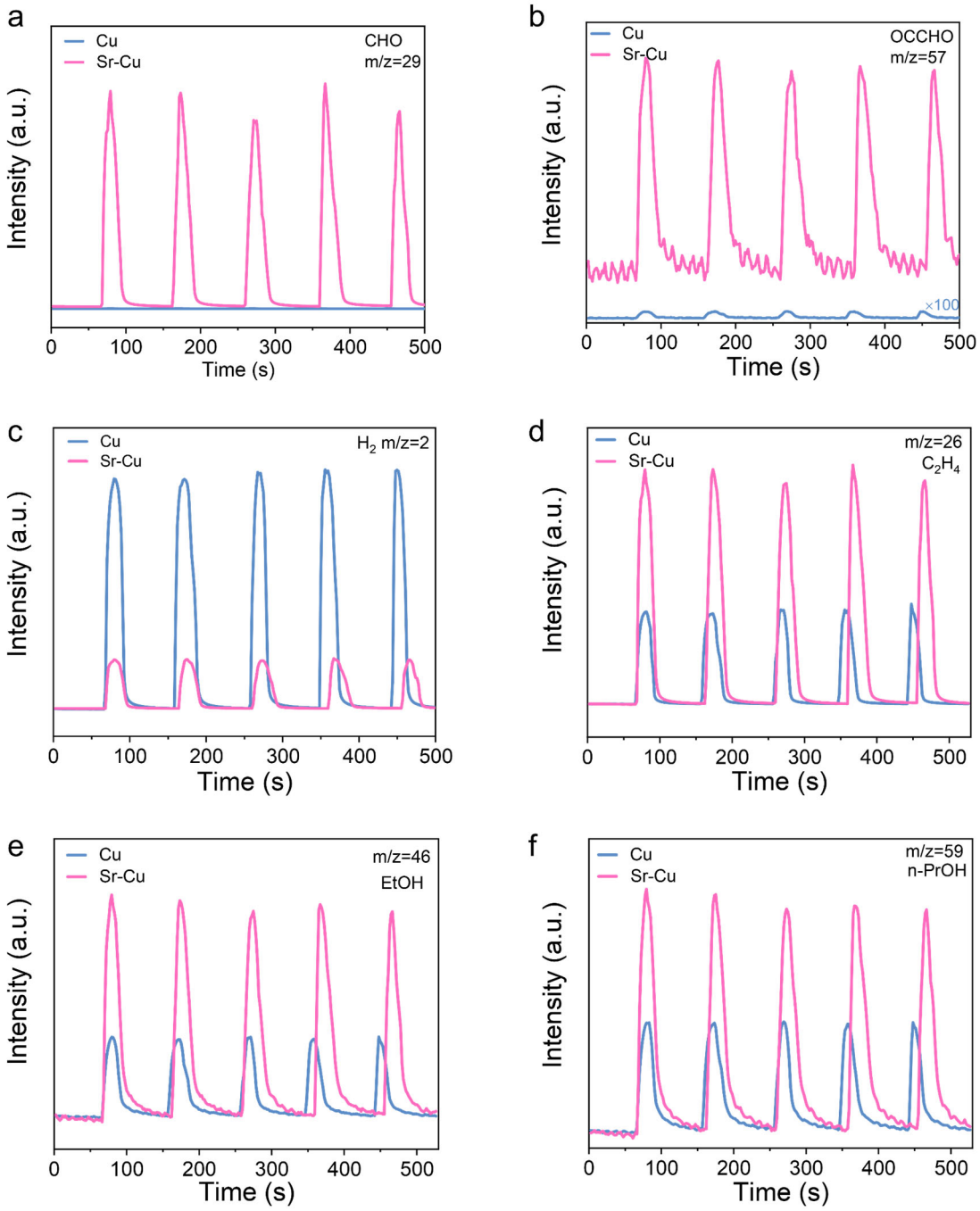

Supplementary Fig. 41 | *Operando* DEMS results. The intensity comparison of key species between Cu and Sr-Cu catalysts for **a,** CHO. **b,** OCCHO. **c,** H_2, **d,** C_2H_4, **e,** EtOH, and **f,** *n*-propanol.

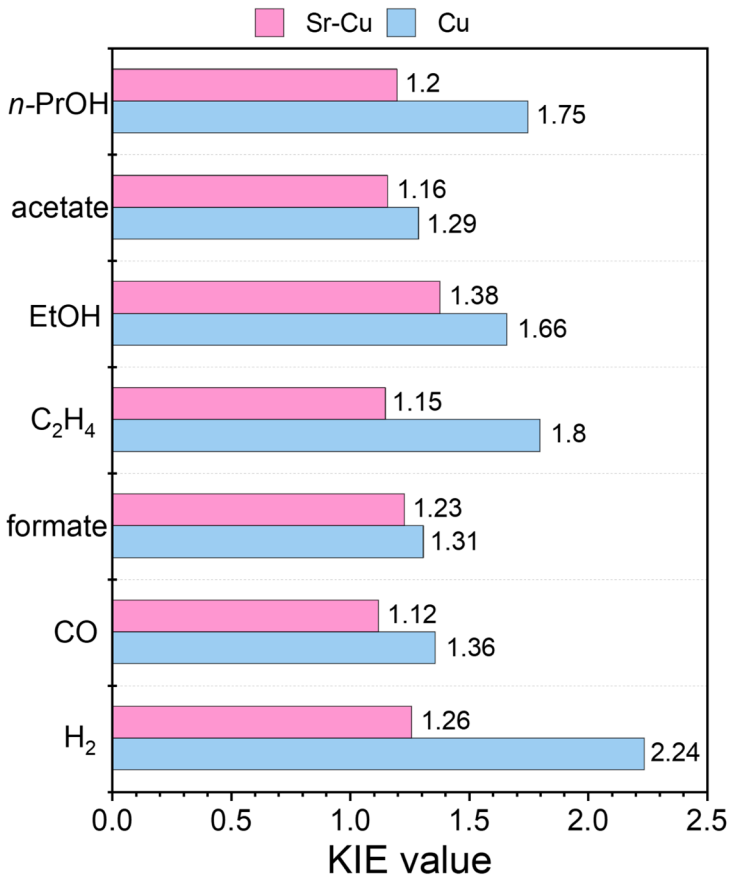

Supplementary Fig. 42 | The kinetic isotope effect of H_2O/D_2O on the Sr-Cu catalyst and Cu catalysts at 1.0 A cm^{-2} current density in flow cell with 1 M KOH. The KIE experiment was conducted by replacing H_2O with D_2O in the electrolyte while keeping the other reaction conditions unchanged, to probe the involvement of proton transfer in the rate-determining process. A more pronounced isotope effect on Cu than on Sr-Cu suggests that proton-coupled elementary steps are more strongly involved on Cu, whereas the Sr-Cu catalyst facilitates C_{2+} formation through a pathway less limited by proton transfer. These results are consistent with the promoted asymmetric C–C coupling pathway on Sr-Cu.

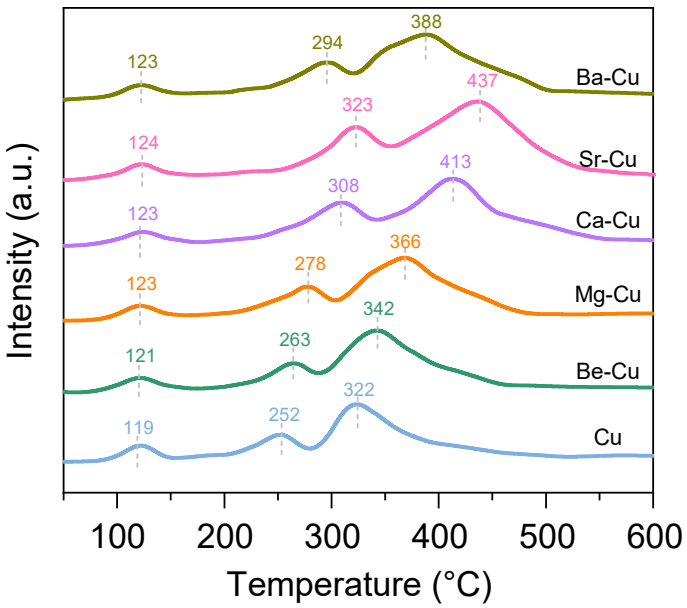

Supplementary Fig. 43 | CO temperature-programmed desorption (CO-TPD) experiments for the X-Cu catalysts. The Sr-Cu catalyst showed TPD peaks at the highest temperature, indicating that the strong binding strength of *CO intermediate, which favors the *CO protonation to *CHO intermediate and the subsequent asymmetric *CO–*CHO coupling to C_{2+} products.

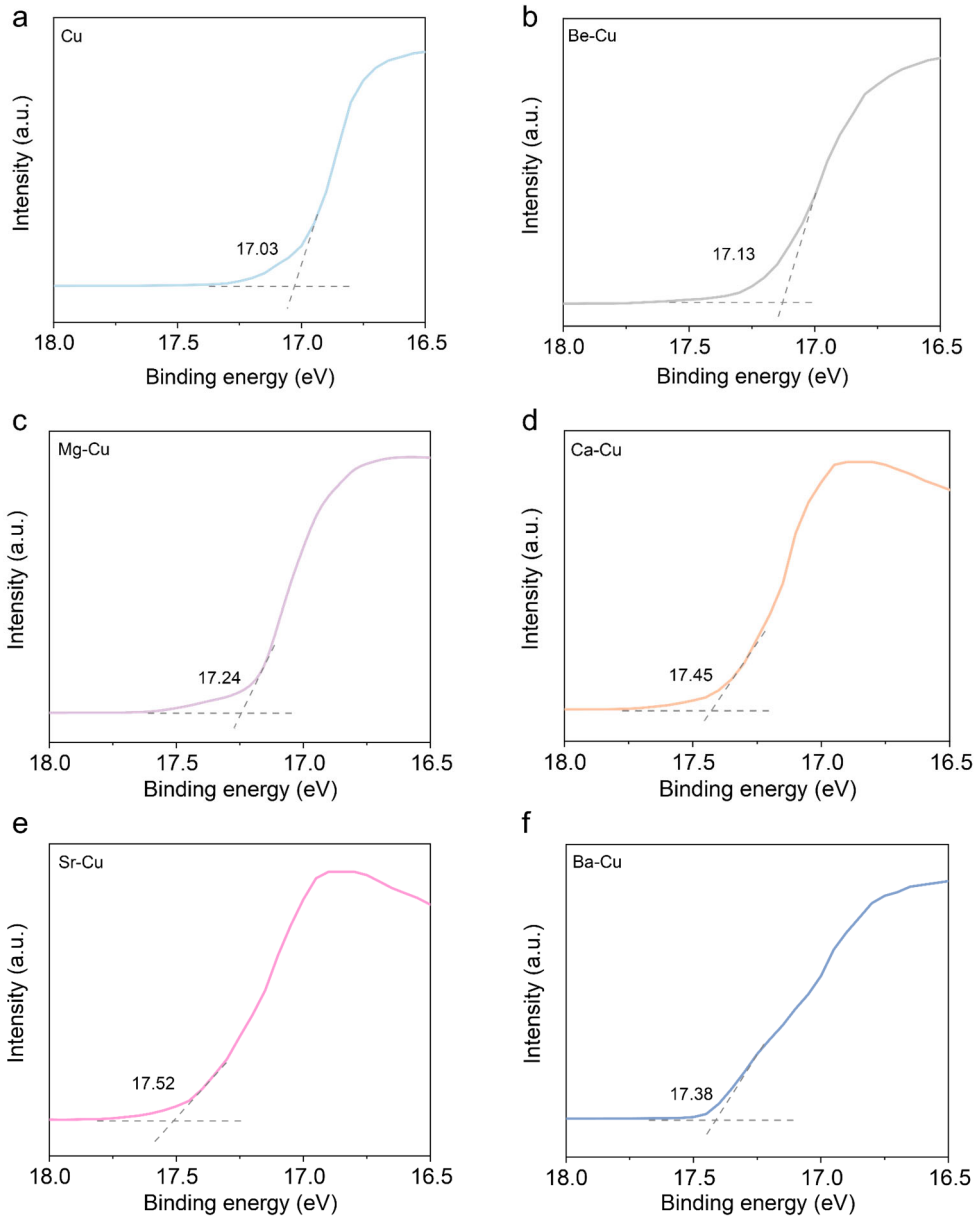

Supplementary Fig. 44 | Work functions of X-Cu catalysts derived from the ultraviolet photoelectron spectroscopy (UPS). The work function (Φ) was calculated using the equation: $\Phi = h\nu - E_{cutoff}$, where hν represents the excitation energy of the He I light source (21.22 eV) and E_{cutoff} is the secondary electron cutoff energy determined from the intersection of the linear extrapolation of the secondary electron cutoff edge with the baseline.

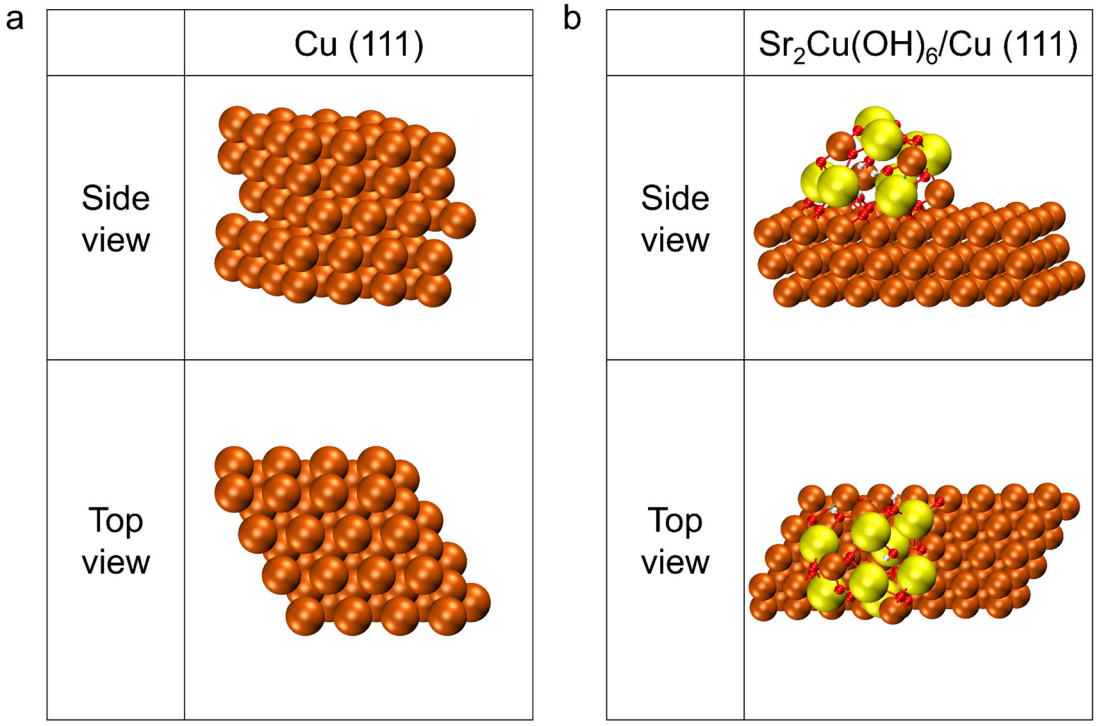

Supplementary Fig. 45 | Side and top views of the Cu(111) and $Sr_2Cu(OH)_6$/Cu(111) model slabs. a, Cu(111). **b,** $Sr_2Cu(OH)_6$/Cu(111). White, red, orange and yellow spheres represent H, O, Cu and Sr atoms, respectively.

	*CO_2	*COOH	*CO
Side view	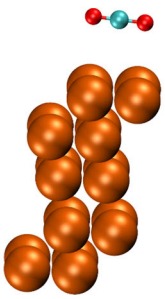	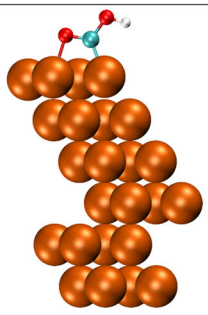	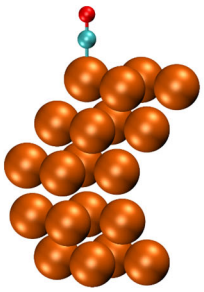
Top view	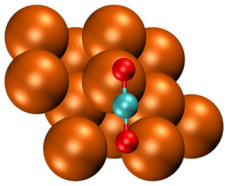	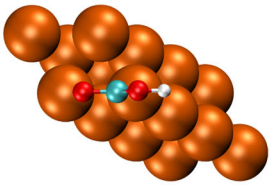	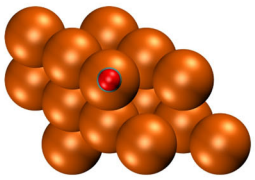

Supplementary Fig. 46 | Side and top views of the adsorbed *CO_2, *COOH, and *CO species on the Cu(111). White, blue, red, and orange spheres represent H, C, O, and Cu atoms, respectively.

	$*CO_2$	*COOH	*CO
Side view	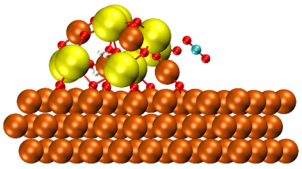	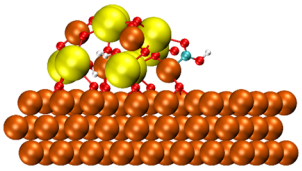	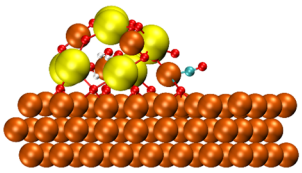
Top view	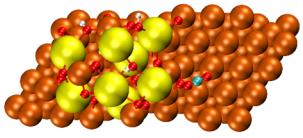	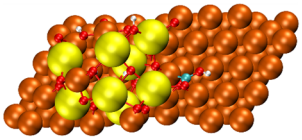	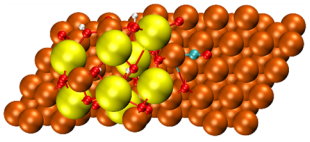

Supplementary Fig. 47 | Side and top views of the adsorbed $*CO_2$, *COOH, and *CO species on the $Sr_2Cu(OH)_6/Cu(111)$. White, blue, red, orange, and yellow spheres represent H, C, O, Cu, and Sr atoms, respectively.

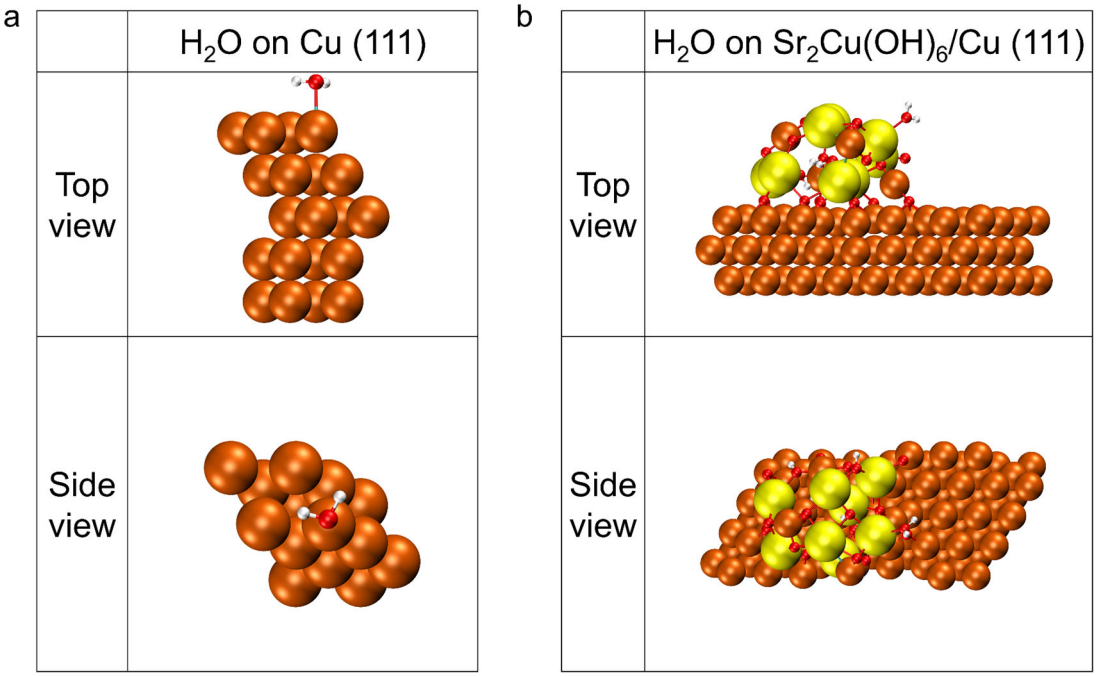

Supplementary Fig. 48 | Side and top views of adsorbed H_2O. a, On the Cu(111). **b,** On the $Sr_2Cu(OH)_6$/Cu(111). White, red, orange and yellow spheres represent H, O, Cu and Sr atoms, respectively.

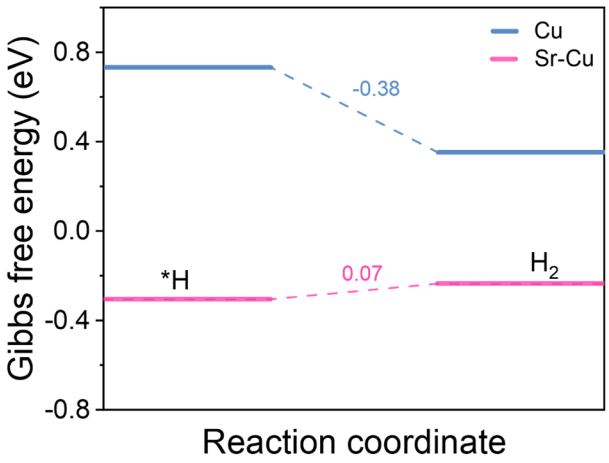

Supplementary Fig. 49 | The reaction energy diagram for the dimerization of *H to H_2. It is noted that the conversion of *H to H_2 is highly exergonic ($\Delta G = -0.38$ eV) on Cu, indicating that the surface protons are prone to recombining into H_2 gas via the hydrogen evolution reaction (HER). In stark contrast, the Sr-Cu surface presents a thermodynamic barrier for H_2 formation ($\Delta G = 0.07$ eV). These results suggest that the HER is effectively suppressed on Sr-Cu. Consequently, the surface *H species are stabilized against self-recombination and are preferentially channeled into the hydrogenation steps of the CO_2RR, thereby promoting the asymmetric *CO–*CHO coupling.

	*CO on Cu (111)	*OCCO on Cu (111)
Side view	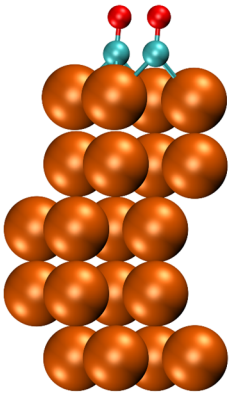	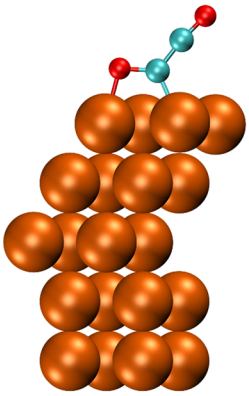
Top view	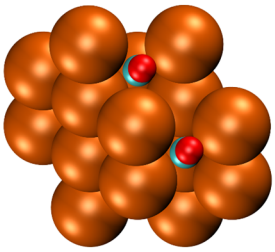	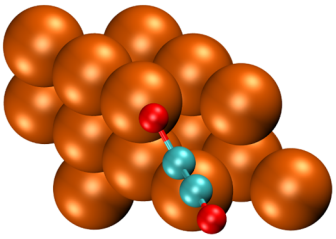

Supplementary Fig. 50 | Side and top views of the initial and final structures during the symmetric *CO–*CO coupling to *OCCO species on the Cu(111). White, blue, red, and orange spheres represent H, C, O, and Cu atoms, respectively.

	*CO on $Sr_2Cu(OH)_6$/Cu (111)	*OCCO on $Sr_2Cu(OH)_6$/Cu (111)
Side view	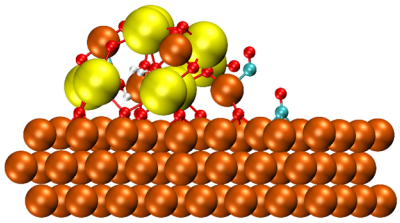	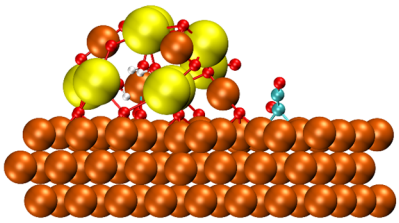
Top view	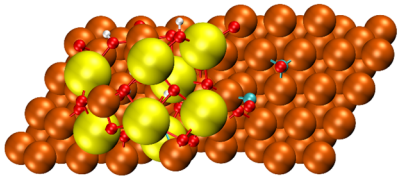	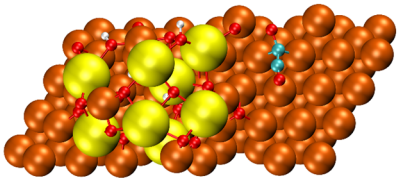

Supplementary Fig. 51 | Side and top views for the initial and final structures during the symmetric *CO–*CO coupling to *OCCO species on the $Sr_2Cu(OH)_6$/Cu(111). White, blue, red, orange, and yellow spheres represent H, C, O, Cu, and Sr atoms, respectively.

	*CO−*CHO on Cu (111)	*OCCHO on Cu (111)
Side view	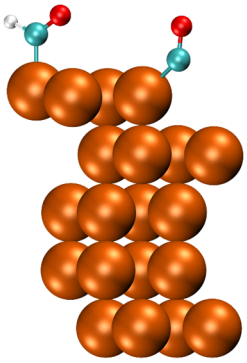	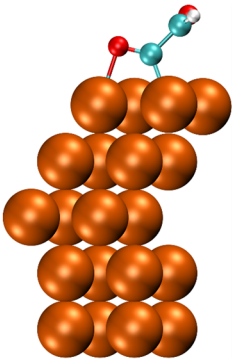
Top view	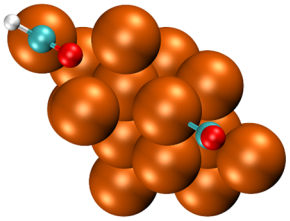	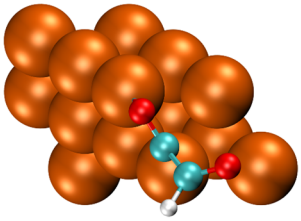

Supplementary Fig. 52 | Side and top views of the initial and final structures during the asymmetric *CO–*CHO coupling to *OCCHO species on the Cu(111). White, blue, red, and orange spheres represent H, O, and Cu atoms, respectively.

	*CO−*CHO on $Sr_2Cu(OH)_6$/Cu (111)	*OCCHO on $Sr_2Cu(OH)_6$/Cu (111)
Side view	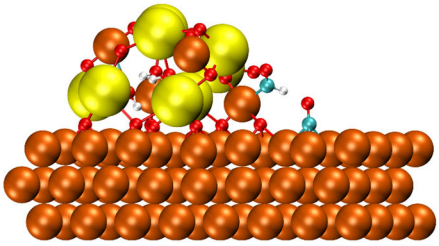	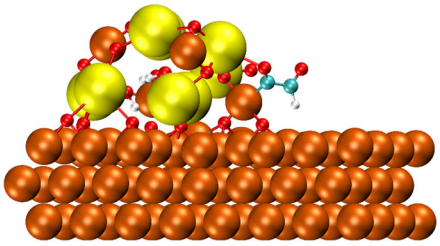
Top view	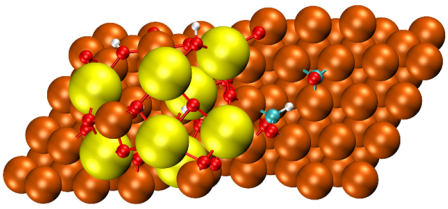	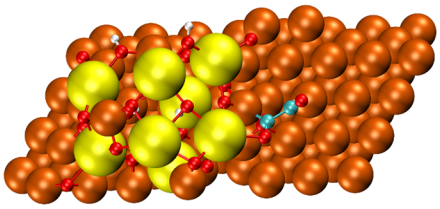

Supplementary Fig. 53 | Side and top views of the initial and final structures during the asymmetric *CO–*CHO coupling to *OCCHO species on the $Sr_2Cu(OH)_6$/Cu(111). White, blue, red, orange, and yellow spheres represent H, C, O, Cu, and Sr atoms, respectively.

Supplementary Table 1 | The molar ratios of water to the key product in some typical cathodic reactions during CO_2RR.

Cathodic reaction	*n* (H_2O) : *n* (product)
$2H_2O + 2e^- \rightarrow H_2 + 2OH^-$	2:1
$CO_2 + H_2O + 2e^- \rightarrow CO + 2OH^-$	1:1
$CO_2 + H_2O + 2e^- \rightarrow HCOO^- + OH^-$	1:1
$2CO_2 + 5H_2O + 8e^- \rightarrow CH_3COO^- + 7OH^-$	5:1
$2CO_2 + 8H_2O + 12e^- \rightarrow C_2H_4 + 12OH^-$	8:1
$2CO_2 + 9H_2O + 12e^- \rightarrow C_2H_5OH + 12OH^-$	9:1
$3CO_2 + 13H_2O + 18e^- \rightarrow C_3H_7OH + 18OH^-$	13:1
$CO_2 + 6H_2O + 8e^- \rightarrow CH_4 + 8OH^-$	6:1

Supplementary Table 2 | Capacitance (C_{dl}), surface roughness factors (R_f) and electrochemical surface area (ECSA) for X-Cu catalysts.

Catalyst	C_{dl} (mF cm^{-2})	R_f[a]	ECSA[b] (cm^2)
Cu	1.1	37.93	37.93
Be–Cu	0.23	7.93	7.93
Mg–Cu	0.19	6.55	6.55
Ca–Cu	0.18	6.21	6.21
Sr–Cu	0.14	4.83	4.83
Ba–Cu	0.16	5.52	5.52

[a]R_f was estimated from the ratio of double-layer capacitance (C_{dl}) for the working electrode and the corresponding smooth polycrystalline Cu electrode (29 μF cm^{-2}). [b]ECSA = $R_f \times S$, where S represents the geometric area of the electrode (in this work, S = 1 cm^2).

Supplementary Table 3 | Electrocatalytic performances of CO_2 to C_{2+} products over typical catalysts reported recently.

Catalyst	Cell voltage (V)	j (A cm^{-2})	C_{2+} FE (%)	Full-cell C_{2+} ECE (%)	Reference
$Cu_2P_2O_7$–derived Cu	3.36	0.35	73.6	25.8	[1]
Thiadiazole-functionalized Ag-Cu	4.5	0.33	80	20.3	[2]
Sputtering Cu	3.8	0.15	80	20	[3]
TPI-modified Cu	3.9	0.315	70	21	[4]
N-modified Cu	3.8	0.15	70	22.1	[5]
Cu-SiO_x	4.2	0.33	80	24.8	[6]
Porous Cu	3.45	0.8	72	24.4	[7]
$Cu_2O/Ag_{2.3\%}$	4.75	0.8	78	18.7	[8]
CuO nanosheets-derived Cu	3.55	0.6	80	26.1	[9]
Cu_2O-Cu^0	3.8	1.0	80	24.7	[10]
Sr-Cu	2.08	0.1	54.2	29.7	This work
	2.29	0.2	65.4	32.6	
	2.44	0.3	75.3	35.4	
	2.54	0.4	78.7	35.5	
	2.78	0.6	83.9	35.0	
	3.03	0.8	86.7	33.2	
	3.28	1.0	92.3	32.5	
	3.79	1.2	87.5	27.0	

Supplementary Table 4 | Thermodynamic potentials (ΔE^0) for some typical full cell electrocatalytic conversions of CO_2 and H_2O.

Full cell reaction	ΔE^0
$2H_2O \rightarrow 2H_2 + O_2$	1.23
$2CO_2 \rightarrow 2CO + O_2$	1.34
$CO_2 + 2OH^- \rightarrow 2HCOO^- + O_2$	1.42
$2CO_2 + 2H_2O \rightarrow C_2H_4 + 3O_2$	1.17
$CO_2 + 2H_2O + 2OH^- \rightarrow 2CH_3COO^- + 2O_2$	1.11
$2CO_2 + 3H_2O \rightarrow C_2H_5OH + 3O_2$	1.15
$6CO_2 + 8H_2O \rightarrow 2C_3H_7OH + 9O_2$	1.13

Supplementary Table 5 | Techno-economic model parameters.

Input Costs	Value	Source
CO_2 (USD/tonne)	30.00	[11]
Water (USD/tonne)	5.00	[12]
Electricity (USD/kWh)	0.01	[13]
KOH (USD/tonne)	790.00	[12]
Electrolyte Concentration (M)	1.0	This work
Target Production of Ethylene (tonne day^{-1})	100.00	This work
Electrolyzer Performance	–	
Ethylene Faradaic Efficiency (%)	68.63	This work
Current density (mA cm^{-2})	1000.00	This work
Cell voltage (V)	3.38	This work
Single Pass Rate (%)	10	–
Plant Parameters		
Reference Electrolyzer Cost (USD/kW)	550.00	[13,14]
Reference Current Density (mA cm^{-2})	400.00	[12]
Balance of Plant, BOP (%)	50	[11,12]
Lang Factor	1	[12,13]
Capacity Factor (%)	90	[12,13]
Electrolyzer Lifetime (years)	20	[12,13]
Catalyst + Membrane Lifetime (years)	5	[12,13]
Catalyst + Membrane Cost/Electrolyzer Cost (%)	5	[12,13]
Electrolyte Lifetime (years)	1	[12,13]
Discount Rate (%)	7	[12,13]
Maintenance Frequency ($year^{-1}$)	5	[12,13]
Maintenance Factor (%)	10	[12,13]
Anolyte Volume (L m^{-2})	100	[12,13]
Gas Separation		

PSA Operational Cost (kW m^{-3})	0.25	[14,15]
PSA Reference Capital Cost (USD)	1989043.00	[14,15]
PSA Reference Capacity (m^3 h^{-1})	1000	[14,16]
PSA Capacity Scaling Factor	0.7	[14,16]

Supplementary Table 6 | Work function of X-Cu catalysts derived from ultraviolet photoelectron spectroscopy.

Catalyst	Work function (eV)
Cu	4.19
Be-Cu	4.09
Mg-Cu	3.98
Ca-Cu	3.77
Sr-Cu	3.7
Ba-Cu	3.84

Supplementary Table 7 | The free-energy values of CO_2, $*CO_2$, *COOH, and *CO on Cu and Sr-Cu.

	Cu	Sr-Cu
CO_2	0	0
$*CO_2$	0.26	0.09
*COOH	0.66	0.53
*CO	0.12	−0.04

Supplementary Table 8 | The free-energy values of H_2O, $*H_2O$, and *H on Cu and Sr-Cu.

	Cu	Sr-Cu
H_2O	0	0
$*H_2O$	0.33	0.18
*H	0.73	−0.31

Supplementary Table 9 | The free-energy values of *CO, *CHO, *OCCO, and *OCCHO on Cu and Sr-Cu.

	Cu	Sr-Cu
*CO	0	0
*CHO	0.71	0.56
*OCCO	1.23	0.64
*OCCHO	0.54	0.19

Supplementary References

1 Sang, J. *et al.* A reconstructed $Cu_2P_2O_7$ catalyst for selective CO_2 electroreduction to multicarbon products. *Angew. Chem. Int. Ed.* **134**, e202114238 (2022).

2 Wu, H. *et al.* Improved electrochemical conversion of CO_2 to multicarbon products by using molecular doping. *Nat. Commun.* **12**, 7210 (2021).

3 Gabardo, C. M. *et al.* Continuous carbon dioxide electroreduction to concentrated multi-carbon products using a membrane electrode assembly. *Joule* **3**, 2777–2791 (2019).

4 Ozden, A. *et al.* High-rate and efficient ethylene electrosynthesis using a catalyst/promoter/transport layer. *ACS Energy Lett.* **5**, 2811–2818 (2020).

5 Kim, J.-Y. *et al.* Quasi-graphitic carbon shell-induced Cu confinement promotes electrocatalytic CO_2 reduction toward C_{2+} products. *Nat. Commun.* **12**, 3765 (2021).

6 Li, J. *et al.* Silica-copper catalyst interfaces enable carbon-carbon coupling towards ethylene electrosynthesis. *Nat. Commun.* **12**, 2808 (2021).

7 Li, W. *et al.* Bifunctional ionomers for efficient co-electrolysis of CO_2 and pure water towards ethylene production at industrial-scale current densities. *Nat. Energy* **7**, 835–843 (2022).

8 Wang, P. *et al.* Boosting electrocatalytic CO_2–to–ethanol production via asymmetric C–C coupling. *Nat. Commun.* **13**, 3754 (2022).

9 Wei, P. *et al.* Coverage-driven selectivity switch from ethylene to acetate in high-rate CO_2/CO electrolysis. *Nat. Nanotechnol.* **18**, 299–306 (2023).

10 He, X. *et al.* Roles of copper (I) in water-promoted CO_2 electrolysis to multi-carbon compounds. *Nat. Commun.* **15**, 9923 (2024).

11 Ozden, A. *et al.* Cascade CO_2 electroreduction enables efficient carbonate-free production of ethylene. *Joule* **5**, 706–719 (2021).

12 Jin, J. *et al.* Constrained C_2 adsorbate orientation enables CO-to-acetate electroreduction. *Nature* **617**, 724–729 (2023).

13 Wang, X. *et al.* Efficient electrosynthesis of n-propanol from carbon monoxide using a Ag–Ru–Cu catalyst. *Nat. Energy* **7**, 170–176 (2022).

14 Shin, H., Hansen, K. U. & Jiao, F. Techno-economic assessment of low-temperature carbon dioxide electrolysis. *Nat. Sustain.* **4**, 911–919 (2021).

15 Jing, X., Li, F. & Wang, Y. Assessing the economic potential of large-scale carbonate-formation-free CO_2 electrolysis. *Catal. Sci. Technol.* **12**, 2912–2919 (2022).

16 Jouny, M., Luc, W. & Jiao, F. General techno-economic analysis of CO_2 electrolysis systems. *Ind. Eng. Chem. Res.* **57**, 2165–2177 (2018).